

Genkwanin glycosides from the *Phaleria nisidai* extract improve glucose homeostasis by stimulating insulin-independent glucose uptake.

Carla Horváth

Swiss Federal Institute of Technology in Zurich

Joelle Houriet

University of Geneva

Caroline Moser

ETH Zurich

Lucia Balazova

Swiss Federal Institute of Technology in Zurich

Miroslav Balaz

ETH Zürich

Hua Dong

ETH Zurich <https://orcid.org/0000-0002-8235-726X>

Aron Horvath

University of Zürich

Vissarion Efthymiou

ETH Zürich

Adriano Rutz

University of Geneva

Laurence Marcourt

University of Geneva

Chris Kitalong

Pacific Academic Institute for Research

Bertrand Graz

University of Geneva

Victor Yano

Pacific Academic Institute for Research

Emerson Queiroz

University of Geneva

Jean-Luc Wolfender

University of Geneva

Christian Wolfrum (✉ christian-wolfrum@ethz.ch)

Article

Keywords: Phaleria nisidai decoction, reverse pharmacology, genkwanin flavone glycosides, adipose tissue, glucose uptake, glucose transporter 1 (GLUT1), insulin sensitivity

Posted Date: March 17th, 2022

DOI: <https://doi.org/10.21203/rs.3.rs-1441076/v1>

License:   This work is licensed under a Creative Commons Attribution 4.0 International License.
[Read Full License](#)

Genkwanin glycosides from the *Phaleria nisidai* extract improve glucose homeostasis by stimulating insulin-independent glucose uptake.

Carla Horvath^{1§}, Joëlle Houriet^{2,3§}, Caroline Moser¹, Lucia Balazova^{1,4}, Miroslav Balaz^{1,4}, Hua Dong¹, Aron Horvath⁵, Vissarion Efthymiou¹, Adriano Rutz^{2,3}, Laurence Marcourt^{2,3}, Christopher Kitalong⁶, Bertrand Graz^{3,6,7}, Victor Yano⁶, Emerson Ferreira Queiroz^{2,3}, Jean-Luc Wolfender^{2,3*} and Christian Wolfrum^{1*}

¹ *Institute of Food, Nutrition and Health, ETH Zurich, Schorenstr. 16, 8603 Schwerzenbach, Switzerland*

² *School of Pharmaceutical Sciences, University of Geneva, CMU, Rue Michel Servet 1, 1211 Geneva, Switzerland*

³ *Institute of Pharmaceutical Sciences of Western Switzerland, University of Geneva, CMU, Rue Michel Servet 1, 1211 Geneva, Switzerland*

⁴ *Institute of Experimental Endocrinology, Biomedical Research Center of the Slovak Academy of Sciences, Bratislava, Slovakia.*

⁵ *Institute of Biomechanics, ETH Zurich, Balgrist Campus, Switzerland*

⁶ *Pacific Academic Institute for Research, 822 Ernguul Rd., Koror, Palau*

⁷ *Antenna Foundation, Avenue de la Grenade 24, 1207 Geneva, Switzerland*

§These authors contributed equally.

*Corresponding authors: christian-wolfrum@ethz.ch and jean-luc.wolfender@unige.ch.

Summary

Natural remedies are used as stand-alone treatments or as additives to modern medicine to control hyperglycemia. Here, we investigate the antidiabetic potential of the Palauan traditional leaf decoction of *Phaleria nisidai* (PNe) using a reverse pharmacology approach. In diet induced obese mice, dietary supplementation with PNe improves insulin sensitivity and promotes glucose uptake into adipose depots. *In vitro*, PNe triggers insulin-independent glucose disposal into murine and human adipocytes by upregulating *Glut1* expression via PKC-ERK1/2 signaling. To identify PNe active principle(s), bioactivity-guided fractionations were performed. We decipher the genkwanin flavone glycosides as active principles found in PNe and demonstrate that the aglycone genkwanin (GE) improves insulin resistance to a comparable extent to metformin. We present GE as promising gluco-regulatory phytochemical, which stimulates baseline glucose uptake into metabolically active adipocytes, thus dampening systemic glucose load and restoring insulin sensitivity.

Keywords: *Phaleria nisidai* decoction, reverse pharmacology, genkwanin flavone glycosides, adipose tissue, glucose uptake, glucose transporter 1 (GLUT1), insulin sensitivity

Introduction

Global diabetes prevalence has quadrupled since 1980, causing reduced life quality and life expectancy. Type 2 diabetes mellitus (T2DM) accounts for 90-95% of diabetes cases, with obesity being the strongest risk factor (NCD Risk Factor Collaboration (NCD-RisC), 2016). Defective blood glucose clearance mechanisms contribute to hyperglycemia, the hallmark of T2DM (Kahn et al., 2006). In healthy skeletal muscle and adipose tissue, glucose transporter 4 (GLUT4) ensures the efficient removal of postprandial glucose in response to insulin. However, impaired insulin signaling leads to dysfunctional GLUT4 shuttling from intracellular vesicles to the plasma membrane (PM) and blunted glucose influx through GLUT4 (Garvey et al., 1998; Tremblay et al., 2001). Apart from GLUT4, adipocytes and myocytes express the insulin-independent glucose transporter 1 (GLUT1), whose physiological relevance in systemic glucose homeostasis is less well studied (Chadt and Al-Hasani, 2020). Corresponding tissue-specific knockout mice have not been characterized and homozygous GLUT1-null mice are not viable, while global heterozygous GLUT1 deficiency results in a high degree of still birth and severe developmental impairment (Heilig et al., 2003). In skeletal muscle, reduced GLUT1 protein levels are observed in insulin-resistant individuals leading to blunted basal glucose uptake (Ciaraldi et al., 2005; Kahn et al., 1991). An equivalent reduction in baseline glucose uptake has been reported in white adipose depots of Wistar fatty rats and tissue explants isolated from obese humans (Ishino et al., 2017; Stolic et al., 2002). Various chemical or hormonal cues can promote GLUT1 PM-translocation and glucose entry into the cell. For example, β 3-adrenergic stimulation of brown adipocytes induces mTORC2 dependent GLUT1 PM-incorporation and insulin has been reported to mildly triggers GLUT1 shuttling in 3T3-L1 adipocytes (Olsen et al., 2014; Yang et al., 1992). In endothelial cells, PKC phosphorylates GLUT1 at S226 in response to VEGF, which targets GLUT1 to the PM and facilitates glucose uptake (Lee et al., 2015). Similarly, the PKC agonist PMA has been shown to stimulate glucose disposal into 3T3-L1 adipocytes by upregulating *Glut1* expression and by

increasing GLUT1 surface levels (Bosch et al., 2004). Taken together, these examples illustrate that GLUT1 in adipose tissue and skeletal muscle might have an impact on glucose homeostasis and represents a poorly investigated route to mitigate hyperglycemia.

Diabetic patients rely on pharmacotherapy to achieve glycemic control. Modern T2DM drug classes like SGLT2-inhibitors, biguanides or GLP1-receptor agonists originate from natural products (Shen, 2015). Due to necessity or choice, populations worldwide use medicinal plants to treat diseases, which provide a valuable pool of potentially bioactive compounds. However, the effectiveness and chemical composition of such remedies are rarely evaluated (World Health Organization, 2013). Reverse pharmacology describes a drug discovery process, which prioritizes traditional knowledge and human clinical efficacy followed by chemical characterization, bioactivity assays and mode of action studies in suitable disease models to discover active substances and define a lead compound (Willcox et al., 2011). A main argument in favor of this approach is that the clinical evaluation in terms of safety and efficacy is carried out before laboratory studies, which increases the chances to pinpoint a constituent with drug-like quality.

The Republic of Palau is heavily affected by obesity and initiated the search for local remedies against metabolic disorders through scientific validation prior to 2007. A program was launched in 2013 to identify currently used Palauan therapies as antidiabetic interventions based on the population's traditional habits. A retrospective-treatment outcome study highlighted a putative effect of the *Phaleria nissidai* Kaneh. (Thymelaeaceae) leaf decoction on glycaemia (Graz et al., 2015) and a subsequent randomized, double-blind crossover trial confirmed this decoction as an adjuvant to stabilize diabetic patients with insufficient glycemic control (Kitalong et al., 2017). Here, we report that the *Phaleria nissidai* leaf extract (PNe) compensates insulin resistance in diet-induced obese mice by elevating insulin-independent glucose uptake into adipose depots via GLUT1. Additionally, we identify genkwanin glycosides as the major active components, which confers the antidiabetic properties of this plant decoction and improves glucose homeostasis with a similar efficacy as metformin.

Results

Dietary supplementation with a PN extract (PNe) improves glucose homeostasis in DIO mice

Based on previous findings, which have reported an antidiabetic effect for PN (Kitalong et al., 2017), we first aimed to reproduce the beneficial effects of PN on glucose control using a diet induced obese (DIO) mouse model paired with a dietary intervention (DI) (Figures S1A-B). To closely adapt the traditional PN preparation in Palau and preserve its chemical composition, a leaf decoction was prepared and freeze-dried to generate the PN extract (PNe). After an initial high fat diet (HFD) feeding period of 12 weeks (Figure 1A), obese and insulin resistant animals were randomly allocated to weight matched groups and subsequently fed control HFD or HFD enriched with the PN extract (130 mg/kg body weight (BW)). The mouse dose was calculated from an estimated human intake of 50 mg/kg BW using the human equivalent dosage formula which corresponded to a lyophilized decoction dose of 10.5 mg/kg*day (Nair and Jacob, 2016). Food intake measurements showed that there was no food aversion due to PNe supplementation (Figure S1C). In accordance with the reported human data (Kitalong et

al., 2017), we did not observe a difference in weight gain or body composition between the two groups (Figures 1B-D), however, PNe-fed mice were more insulin sensitive after 5 weeks of DI (Figures 1E-F). PN feeding reduced fasting insulin (Figure 1G) concentrations without altering fasting blood lipid parameters (Figures 1H-J). Although PNe did not significantly improve oral glucose tolerance after only two weeks intervention (Figures 1K-L), we detected lower glucose-stimulated plasma insulin concentrations 30 min after an oral glucose load (Figure 1M), which supports an improvement in insulin sensitivity (Wang et al., 2019). PNe furthermore dampened urinary glucose excretion (Figure 1N). To evaluate a possible short-term activity of PNe we examined the glucoregulatory response to single oral dose of PNe (130 mg/kg BW) in mice fed with HFD for 10 days. PNe administration lowered blood glucose concentrations after 4 hours when compared to vehicle controls (Figures 1O-P), indicating that PNe triggers glucose clearance independently of insulin. As we could show that PN regulates systemic glucose homeostasis, we investigated if PN-supplementation increases glucose uptake into metabolically relevant tissues using ¹⁴C-2-deoxyglucose tracing and counted accumulated phospho-deoxyglucose in the basal state. We did not detect a difference in glucose disposal into skeletal muscles or liver (Figures 1Q-S). However, higher amounts of glucose uptake were observed in inguinal white adipose tissue (iWAT) and interscapular brown adipose tissue (iBAT) (Figure 1T-U), but not in the epididymal depot (eWAT) (Figure 1V). The combined results from the chronic and acute PNe treatment regimens, suggest that PNe acts on blood glucose concentrations, by directly stimulating signaling pathways and/or by inducing a long-term adaptive response cumulating in improved insulin sensitivity.

PNe promotes glucose uptake by upregulating GLUT1 protein in adipocytes

To gain insights into the molecular mechanisms underlying the elevated insulin sensitivity observed *in vivo* and considering our glucose tracing data, we assessed the effect of PNe on adipocyte glucose metabolism using immortalized murine white and brown adipocyte cell lines (Figure 2A). After 3 days of daily PNe treatment (200 µg/mL), we measured higher insulin-stimulated (60 min) ¹⁴C-2-deoxyglucose uptake into white (Figure 2B) and brown (Figure 2C) adipocytes. Interestingly, we noted a 30% increase in insulin-independent glucose disposal (Figure 2B-C). These measurements suggest that PNe does not primarily act on the insulin-dependent arm of glucose clearance but rather boosts basal glucose uptake. Consistent with augmented baseline glucose uptake, GLUT4 protein content was unchanged by PNe, whereas GLUT1 protein was upregulated (Figures 2D-H). To further exclude that PNe acts via insulin responsive GLUT4, we examined the phosphorylation state of Protein Kinase B (AKT) at S474 and T308, which link insulin signaling to GLUT4 plasma membrane translocation. Both phosphor-sites were not affected by PNe exposure at baseline or insulin-stimulated conditions (Figures 2I-M), demonstrating that increased glucose disposal is due to an insulin independent mechanism. To assess post-uptake metabolization, we calculated glycolysis from the extracellular acidification, which demonstrated that PNe dose-dependently increased glycolysis as well as glycolytic capacity (Figure 2N-O). To substantiate these findings, we directly measured glycolytic flux using ³H-labelled glucose. We could corroborate that PNe treatment for 3 days significantly enhanced glycolytic rate by more than 25% (Figure 2P-Q). A concurrent upregulation of glycolytic genes including *Pfkm*, *Pdk* or *Pgk* (Figure 2R-S) underlines that PNe not only promotes adipocyte glucose uptake but also glucose utilization. In

addition, we detected an upregulation of *Glut1* mRNA expression in response to PNe treatment (Figures 2R-S). Taken together, these data imply that the described elevation in GLUT1 protein levels possibly derives from increased *Glut1* transcription. We could translate these findings to our animal model system, where we detected higher GLUT1 but not GLUT4 protein content in the iWAT and iBAT of PNe-fed animals compared to HFD controls (Figure 2T-V). As PN is effective in humans, we tested the extract on human white and brown differentiated adipocytes (hMADS) and we could validate increased GLUT1 protein levels stimulated by PNe (Figure 2W-Y). This was paralleled by a 38% increase in basal glucose uptake rates in brown hMADs that was sustained in the insulin-stimulated condition (Figure S2A). Furthermore, the dose-dependent enhancement of glycolysis and glycolytic capacity in human adipocytes (Figure S2B-C) was similar to the murine system. Collectively, our findings from murine and human adipocytes indicate that PNe increases insulin-independent glucose uptake, possibly by increasing GLUT1 protein levels concomitant with an increased glycolysis.

Short-term PNe treatment increases adipocyte glucose uptake by activating the PKC-pGLUT1 axis

As a single bolus of PNe was sufficient to elicit a glucose lowering response in mice, we next examined the effects of short-term PNe exposure on adipocyte glucose uptake. Stimulation of white and brown adipocytes with PNe for 3 hours was sufficient to enhance glucose uptake in the basal state, which was accompanied by higher insulin-dependent glucose disposal (Figures 3A-B). In agreement with the observations from the long-term experiments, pAKT levels were unaffected (Figures 3C-G). As it has been reported that activated protein kinase C (PKC) can upregulate *Glut1* mRNA and protein levels in response to various stimuli, leading to higher glucose uptake rates (Bosch et al., 2004; Montessuit and Thorburn, 1999; Nose et al., 2003), we hypothesize that PNe could exert its function via PKC signaling. Indeed, we could show that PNe increased the phosphorylation of various PKC substrates (Figure 3H) while levels of pPKC substrates were decreased when cells were pre-exposed to the PKC inhibitor Gö-6983 for 30 min (Figure S3A). Lee et al., have reported a PKC-dependent phosphorylation of GLUT1 at S226 in endothelial cells using the PKC agonist PMA, which promoted GLUT1 plasma membrane shuttling and concomitant glucose uptake (Lee et al., 2015). We next tested whether PNe activates PKC, resulting in GLUT1-phosphorylation and augmented glucose uptake. We could verify that administrating PNe for 15 min caused GLUT1 phosphorylation at S226 in both brown and 3T3-L1 adipocytes, which was maintained for up to 3h of stimulation (Figure 3J-L). In turn, blockage of PKC activity by pre-treating the cells with the PKC inhibitor Gö-6983 prevented the PNe-induced phosphorylation of GLUT1, which highlights the PKC-dependency of this phosphorylation event (Figure 3M). More importantly, the increase in glucose uptake triggered by an acute PNe-dose was abolished when PKC was inhibited (Figure 3N).

ERK1/2 is a downstream target of PKC which translocates to the nucleus after phosphorylation, where it was shown previously to regulate *Glut1* gene transcription (Bosch et al., 2004; Ge et al., 2011). We predicted that the increase in GLUT1 protein content observed in the chronic PNe treatment regime is mediated through the sequential activation of ERK1/2 signaling by PKC and upregulation of *Glut1*

expression. PNe triggered ERK1/2 phosphorylation in murine (Figures 3O-P) and human (Figures S3B-C) brown adipocytes. Moreover, 4 hours of PNe treatment significantly increased *Glut1* mRNA expression, which was abrogated when cells were pre-exposed to the ERK1/2 inhibitor (Figure 3Q). To substantiate these findings, we performed immunofluorescence staining and visualized a predominant nuclear localization of ERK1/2 in response to PNe. In contrast, ERK1/2 remained localized in the cytosol, when PKC was inhibited by Gö-6983 (Figures 3R-S). Lastly, suppression of ERK1/2 prevented PNe-stimulated glucose uptake after 16 hours of treatment (Figure 3T). In summary, our data demonstrates that PNe acts as a PKC activator, which enables higher glucose uptake by phosphorylating GLUT1 and by initiating *Glut1* transcription by ERK1/2. This mode of action presents an original strategy to target hyperglycemia, since the established diabetes drugs do not target insulin-independent glucose uptake.

A bioactivity-guided fractionation approach reveals other constituents than the major compound mangiferin as functionally relevant

We subsequently focused on identifying the active principle, which governs the function of PNe. An initial analysis of the phytochemical composition of PNe using ultra high-performance liquid chromatography with corona-charged aerosol detection (UHPLC-CAD) and high-resolution mass-spectrometry (UHPLC-HRMS/MS) identified the xanthone mangiferin (MG) as the main constituent present in PNe-(Figures S4A). The MG level measured in PNe was of $14.5 \pm 0.4\%$ ($n=4$), which is consistent with earlier chemical profiles of PN (Kitalong et al., 2017). Furthermore, Apontes et al., have previously described in detail the anti-hyperglycemic activity of MG (Apontes et al., 2014). To assess whether MG recapitulates the activity of PNe *in vitro*, we treated white or brown adipocytes for 3 days with MG. Unexpectedly, MG did not alter basal or insulin-stimulated glucose uptake rates (Figures S4C-D), suggesting that other compounds than the main PNe constituent should be functionally relevant.

To explore potentially active principles in the PN extract, we fractionated the extract in four fractions (F1-F4) (Figures S4 and S5A). F1 contained polar compounds (mainly saccharides) (Figures S4B and S5A), F3 consisted of MG and iriflophenone-2-O- β -glucoside (Figures S4C and S5A-B), while F2 and F4 corresponded to fractions devoid of MG (Figures S4D-E and S5A-B). Fractions F2, F3 and F4 were tested *in vivo* concomitantly with PNe after an initial HFD-feeding regime of 6 weeks (Figure 4A) with doses corresponding to the amounts found in total PNe (see Star Methods section: "Fraction preparation and dosage for *in vivo* testing"). As chronic intake of complex plant preparations can cause herbal-induced-liver injury (Licata et al., 2013), we quantified plasma alanine transaminase (ALT) levels in response to the fractions and PNe (de Boer and Sherker, 2017). After 12 weeks of exposure, none of the applied fractions or the extract induced higher plasma ALT activity (Figure S6A). Furthermore, no differences in food intake patterns (Figure S6B), body weight development (Figures S6C-D) or composition (Figure S6E) were observed between groups similar to PNe (Figure 1B). All fractions lowered random fed blood glucose (RBG) concentrations during the DI with most pronounced effects for F4 (Figure 4B). All investigated fractions improved insulin sensitivity (Figure 4C-D) after 4 weeks of treatment, while only F4 effectively ameliorated insulin sensitivity after prolonged DI (Figure 4E-F). F4 and F2 enhanced blood glucose clearance after an oral glucose load (Figure 4G-H). Interestingly, only

F3-fed mice displayed higher circulating active GLP-1 concentrations 2 min after an oral glucose bolus (Figure 4I). In agreement with the observed benefits of PN fractions on glucose homeostasis, terminal fasting blood glucose was reduced in all treatment groups (Fig. 4J). In conclusion, our data demonstrate that all three fractions modulate glucose homeostasis in DIO mice by improving different metabolic readouts, however prolonged insulin sensitivity is only conferred by F4.

To assess the effectiveness of F4 versus a known intervention we compared the efficacy of F4 treatment against the diabetes drug metformin (MET) at a dose of 0.25% w/w (Matsui et al., 2010) (Figure 4K). Over the course of the DI, F4 and MET lowered RBG to a similar extent (Figure S7A). This reduction in blood glucose is not due to inhibition of intestinal alpha glucosidase activity, as the magnitude and rate of appearance of blood glucose spikes did not differ between groups in an oral sucrose tolerance test (Figure S7B-C). In turn, insulin sensitivity was improved by F4 after 9 weeks of DI (Figures S7D-E). To quantify the improvement in insulin sensitivity caused by F4 intake and to decipher the responsible tissues more precisely, we performed hyperinsulinemic-euglycemic clamps (Figure 4K) after 7 to 8 weeks of DI. Compared to control fed animals (36.3 ± 5.7 mg/kg*min), F4 (43.0 ± 6.0 mg/kg*min) and metformin (47 ± 6.4 mg/kg*min) treated mice had a significantly increased glucose infusion rate (GIR, Figure 4L). Glucose infusion rates over time are presented as mean for each group (Figure S7F) and for each mouse within a group (Figures S7G-I). Blood glucose concentrations during the procedure are in (Figure S7J). Basal whole-body glucose turnover (Figure 4M) was not different between the groups but trended to be higher in F4 animals (F4= 13.8 ± 6.3 vs HFD= 9.9 ± 0.89 mg/kg*min). However, during the insulin-stimulated condition glucose turnover was elevated for both, metformin and F4 mice (Figure 4M). Endogenous hepatic glucose output was consistent between all groups, but robustly repressed after insulin infusion (Figure 4N). A single bolus of ^{14}C -2-deoxyglucose was infused into the jugular vein in steady state conditions and tissue-specific glucose uptake rates assessed. iWAT, iBAT, liver and soleus (Figure 4P-S) displayed higher glucose influx for both, metformin and F4 treatments (Figures 4Q-T). Uptake rates into the gastrocnemius (Figure 4T) were higher, but not statistically significant and the eWAT (Figure 4O) was unaffected by either treatment. Overall, we could show that dietary supplementation with F4 has a profound impact on glucose uptake kinetics in various tissues to a slightly lower magnitude than metformin.

Chemical composition of fraction F4

We next aimed to unravel the chemical composition of F4 to specify the constituents conferring its antidiabetic activity. F4 was further fractionated to formally identify its constituents. Chromatographic separation of F4 was optimized to purify seven compounds, which were unambiguously characterized by NMR analyses (see Star Method section: "Description of the isolated compounds", and Figures S4 and S5). Two acetylmangiferins xanthenes were identified; 6'-O-acetylmangiferin (Markham and Wallace, 1980) and 2'-O-acetylmangiferin, which was never reported to our knowledge. Two mangiferin glucofuranosyl-derivatives, 2-C- β -glucofuranosylmangiferin and 2-C- α -glucofuranosylmangiferin, are also described for the first time. The presence of the flavone genkwanin 5-O- β -primeveroside (synonym of yuankanin), already described for PN (Kitalong, C. et al., 2012), was confirmed. The C-glucoside

isovitexin (Pedras et al., 2003), and genkwanin-5-O- β -glucoside (Veit et al., 1990) are reported for the first time in PN.

Since the MG-containing F3 was not as effective as F4 with respect to insulin sensitivity we limited our *in vivo* test to the flavones isovitexin (IX), genkwanin 5-O- β -glucoside (GG) and genkwanin 5-O- β -primeveroside (GP) to identify the active antidiabetic phytochemical. We additionally tested genkwanin (GE), the common aglycone of genkwanin 5-O- β -primeveroside and genkwanin 5-O- β -glucoside as well as apigenin (AP), the aglycone of isovitexin (Figure 5A). Indeed, glycosylated flavonoids are known to be cleaved by intestinal metabolism after ingestion (Németh et al., 2003). The tested concentrations were calculated from the estimated proportions of the individual compounds in PN, assuming that glycosides are converted to their aglycone at a 1:1 ratio (Figure 5B). After 7-8 weeks of DI, insulin sensitivity (Figure 5C-D) and glucose tolerance (Figure 5E-F) were improved following GE and GG treatment. Similarly, RBG was reduced by the end of the intervention (Figure 5G), while the other tested compounds had no impact on glucose homeostasis (Figure 7A-D). Furthermore, GE-treated mice displayed increased urinary glucose concentrations, which indicates higher renal glucose excretion (Figure 5H). Indeed, phloretin is a predicted metabolite of genkwanin and structurally related to phlorizin, the precursor compound of the current SGLT2-inhibitor drug class (Ehrenkranz et al., 2005; Schoefer et al., 2003). In human, a lower visceral to subcutaneous fat ratio is metabolically favorable and correlates with insulin sensitivity (Kaess et al., 2012). While amounts of iWAT and eWAT did not differ between treated and HFD-fed mice (Figure S8E-F), we observed a lower VAT/SAT-ratio in the GE-group (Figure 5I). This finding implies a shift in fat storage into the subcutaneous depot, which might lead to a healthier adipose tissue expansion in response to chronic overnutrition and contribute to improved glucose homeostasis. Furthermore, after four weeks of DI, blood lipid and insulin concentrations remained unchanged in the fasted state (Figures S8G-J). At the end of the intervention, random fed NEFA, cholesterol (Figures S8K-L) and insulin levels (Figure S8N) were likewise indifferent. However, triglyceride concentrations were reduced for GG and IX fed mice (Figure S8M). Comparing the effects of F4 and individual F4 constituents based on the AUC from the GTT, we measured a 19.7% decrease in the AUC from F4 vs HFD animals, a 12.7% decrease for GE vs HFD and a 13.9% for GG vs HFD. Taken together, our data suggest that GE glycosides confer the glucose-sensitizing effects of F4, whereas the other tested compounds did not exert any relevant bioactivity.

Genkwanin promotes insulin sensitivity by stimulating GLUT1 phosphorylation and AKT

The crude PN extract promoted insulin-independent blood glucose clearance into adipose depots by upregulating GLUT1 protein (Figures 1T-U and 2W-Y). Therefore, we determined if GE induced the same molecular pathways. We could confirm a stimulatory effect of GE on glucose uptake into iBAT and iWAT without co-administration of insulin (Figure 6A-B). Glucose disposal into eWAT was unchanged (Figure 6C). In line with enforced insulin-independent glucose disposal, mice supplemented with GE showed higher GLUT1 protein in the iBAT but not iWAT (Figures 6D-E) and a BAT-restricted increase in GLUT1 S226 phosphorylation (Figures 6F-G). Western blots for all targets are shown in Figures 6N-Q. This depot-specific GLUT1-regulation implies that GE acts predominantly on metabolically active brown adipocytes, which exist in form of brite/beige adipocytes in the WAT depot

of mice housed at room temperature (van der Stelt et al., 2017). GLUT4 levels were unaltered in both adipose types (Figures 6H-I). We speculated that a mild but persistent increase in baseline glucose clearance rates might cumulatively lead to a glucose-lowering response, which reduces systemic glucotoxicity and assists in preserving insulin responsiveness. This is suggested by increased AKT phosphorylation at S473 in the random fed state in the iWAT and iBAT of GE fed mice (Figures 6J-K). A simultaneous increase in total AKT levels, detected for GE in iBAT samples, might add to this observation (Figure 6L-M). As one experimentally supported mechanism, we propose that GE operates as glucose sensitizer of metabolically active adipocytes, which secondarily strengthens global insulin-sensitivity.

Genkwanin ameliorates systemic glucose homeostasis comparably to metformin

In a last experiment, we evaluated how genkwanin performs against metformin in the hyperinsulinemic-euglycemic clamp to support its effectiveness (Figure 7A). It needs to be accentuated that the selected GE dosage (3.5 mg/kg BW) originates from nutrition-based intake levels as opposed to metformin supplementation (0.25%), which relates to a pharmacologically relevant human dose. Compared to HFD-controls (25.3 ± 7.7 mg/min*kg BW), MET (39.8 ± 6.7 mg/min*kg BW) and GE (39.8 mg/min*kg BW) supplementation increased glucose infusion rates (Figure 7B-C) required to stabilize blood glucose at 6 mM (Figure 7D). Consistently, GE and MET elevated insulin-stimulated glucose disappearance rate (Figure 7E) and whole-body glucose turnover (Figure 7F) to a comparable extent. Basal glucose turnover (Figure 7F), which equals to basal hepatic glucose production (Figure 7G), was unchanged between treatment groups. Not only insulin-induced glucose clearance was promoted by GE, but also hepatic insulin-sensitivity improved as reflected in stronger suppression of endogenous glucose production (Figure 7G). ^{14}C -deoxyglucose tracing during the last 30 min of the clamps revealed higher glucose disposal rates into the eWAT (Figure 7H), iWAT (Figure 7I), liver (Figure 7K) and soleus (Figure 7L) for both GE and MET, while a trend was observed for iBAT (Figure 7J). No differences were observed in the gastrocnemius (Figure 7M). Together, these data emphasize the therapeutic potential of orally applied genkwanin to treat systemic insulin resistance and restore normal glycaemia.

Discussion

In Palau, the PN leaf extract has been consumed for decades (Kitalong et al., 2012), among other indications, as an herbal antidiabetic agent without formally documented clinical and mechanistic evidence for its efficacy. The plant was selected based on a retrospective treatment outcome survey (Graz et al., 2015), which aimed at evaluating the traditionally used remedies with the best reported outcomes for metabolic and non-communicable diseases. A randomized clinical trial confirmed the efficacy of PNe in humans (Kitalong et al., 2017) and our investigation aimed at identifying the active principles and determining their possible mechanisms of action.

To elucidate possible mechanistic activity, we report here the glucoregulatory effect of PNe in DIO mice and delineated genkwanin glycosides as mediators of the beneficial action of PNe in an interdisciplinary study. A single oral dose of PNe was sufficient to lower blood glucose whereas prolonged food

supplementation elevated insulin sensitivity. Although insulin-stimulated glucose uptake into adipose tissue is 4-5 times lower compared to muscle (Virtanen et al., 2001), the adipose organ is a fundamental regulator of whole body glucose homeostasis as can be seen in adipocyte-specific *Glut4* knockout animals (Abel et al., 2001), which develop insulin resistance in the liver and skeletal muscle causing glucose intolerance. Based on our *in vitro* data from brown and white adipocytes we propose that PNe exerts part of its advantageous effect on glucose metabolism by stimulating of protein kinase C (PKC). Consistent with findings in endothelial cells (Lee et al., 2015), we describe here that the PKC-dependent phosphorylation of GLUT1 at S226 is responsive to PNe in adipocytes. Similarly, the PKC agonist PMA augments glucose disposal into 3T3-L1 adipocytes (Tsuru et al., 2002), which corresponds to our glucose uptake data from an acute PNe dose. A prolonged PNe challenge led to elevated GLUT1 protein content in brown and white adipocytes but also in the corresponding murine fat depots, which emerged from the parallel upregulation of *Glut1* mRNA. This transcriptional regulation of *Glut1* was suppressed when cells were pretreated with an ERK1/2 inhibitor, a known activator of *Glut1* transcription. Incubation of adipocytes with the PKC-agonist PMA initiates *Glut1* expression through active of ERK1/2 (Bosch et al., 2004). Similarly, FGF21 stimulates *Glut1* expression in murine eWAT via the sequential activation of ERK1/2 and the downstream transcription factors SRF/ELK1 (Ge et al., 2011). Based on our *in vitro* findings, we conclude on a dual mode of GLUT1 regulation by PN to ensure proper glucose disposal. PN acutely augments glucose uptake through the phosphorylation of GLUT1 and its redistribution to the plasma membrane. This effect is maintained until the synthesis of *Glut1* is induced via ERK-mediated transcription leading to an adaptive increase in the total GLUT1 pool in response to prolonged PN treatment. Analog regulatory patterns defined by an initial shift of glucose transporters to PM that is strengthened by higher total GLUT abundancy maintain cellular glucose supply in situations of high-energy demand triggered by exogenous or metabolic cues (Kennedy et al., 1999; Khayat et al., 1998; Koivisto et al., 1991; Lund et al., 1995; Ren et al., 1994; Taha et al., 1997). Leveraging insulin-independent glucose clearance is an attractive strategy as it bypasses dysfunctional insulin receptor signaling. Known mechanisms such as AMPK activation (Taylor et al., 2008) and β 2-adrenergic receptor stimulation in skeletal muscle (Kalinovich et al., 2020) promote glucose clearance downstream of the insulin receptor via GLUT4, thereby converging on the same GLUT as insulin-stimulated glucose uptake. *Glut4* expression is reduced in skeletal muscle (Gaster et al., 2001; Kampmann et al., 2011) and adipose tissue of diabetic subjects (Garvey et al., 1991), which might affect their responsiveness to such treatments and contribute the pathology of insulin resistance. In contrast, GE exploits adipocyte GLUT1 to enhance basal glucose disposal, which could open up a novel therapeutic direction to control blood glucose concentrations.

Our mangiferin-guided fractionation strategy exposed that all fractions exert biological activities, which are evident in distinct metabolic parameters and suggest different underlying molecular mechanisms. Due to the chemical complexity of PNe and potential additive, synergistic or antagonistic interactions between substances, we cannot rule out that the observed activities of the fractions are maintained in the whole extract and contribute to PNe's effects. Apontes et al., (Apontes et al., 2014) described the protective effects of a MG-enriched HFD in C57BL6/J mice, which caused reduced weight gain, improved insulin sensitivity and increased energy expenditure due to enhanced carbohydrate utilization

in muscle. Surprisingly, we did not observe a change in bodyweight development and the physiological response to the MG-containing F3 was less pronounced than for F4 although MG is the most abundant constituent in the PN decoction. A plausible explanation for this discrepancy lies in the applied dosages. In our study, MG intake through the PNe equals to 34 mg/kg BW, whereas the dietary supplementation of Apontes et al., results in an approximate dose of 400 mg/kg BW. *In vitro*, MG was shown to exert DPP-4 inhibitory activity and a single-dose of MG was effectual to elevate plasma GLP-1 levels in streptozotocin-induced diabetic rats (Suman et al., 2016). F3 was the only fraction that augmented circulating GLP-1 concentrations after an oral glucose load, which might arise from its weakened or delayed degradation due to DDP4-inhibition by MG.

Metformin is the most frequently prescribed first-line therapy for type 2 diabetes. In our study, the applied metformin concentration (0.25% w/w) translates to a daily human dose of 1300 mg which is within the recommended therapeutic range of 500-2500 mg per day (Corcoran and Jacobs, 2021). In contrast, GE was dosed referring to a daily nutritional exposure by the PN decoction and was not titrated for its full pharmacological response. The results from the hyperinsulinemic-euglycemic clamp emphasize the potency of GE even at this low dose, which had comparable effects on blood glucose to those of metformin. Future dose-response and toxicology studies will be required to determine the maximum dose for GE treatment of diabetes. Although metformin is used as an isolated substance since 1957 (Bailey, 2017), an unambiguous mode of action is still debated. Its glucose-lowering properties are attributed to the modulation of multiple molecular pathways rather than a single drug-target interaction. This is also reflected in the pleiotropic effects described for metformin such as suppression of hepatic gluconeogenesis (Hundal et al., 2000) or stimulation of glucose uptake into skeletal muscle (Zhou et al., 2001) due to alterations in cellular redox homeostasis (Madiraju et al., 2014, 2018), reduced hepatic energy state (Foretz et al., 2010), activation of AMPK (Zhou et al., 2001) or mitochondrial complex I inhibition (Owen et al., 2000). Similarly, we suggest that genkwanin glycosides improve glucose homeostasis, in part by upregulating *Glut1* in metabolically active adipocytes. We speculate that these adipocytes function as glucose sink, which blunts glucotoxicity in other tissues, thereby improving or preserving systemic insulin-sensitivity and safely storing excess glucose in its dedicated organ. GE triggered glucose disposal into the iWAT and BAT but not eWAT and this tissue distribution pattern coincides with the occurrence of brown or beige/brite adipocytes in mice housed at room temperature (Waldén et al., 2012). Very recent data from female BAT-specific Rab10 knockdown mice supports the notion that catabolic adipocytes contribute to systemic glucose metabolism independent of their thermogenic role (Picatoste et al., 2021). Moreover, GE treatment was associated with a decreased eWAT to iWAT ratio indicating that more glucose is directed to the subcutaneous depot causing a shift in fat distribution. This preferential accumulation of subcutaneous rather than visceral fat could additionally impact metabolic health (Kaess et al., 2012; Preis et al., 2010). At least in extreme conditions like long-term cold exposure, stable glucose isotope tracing studies in mice revealed that anabolic and catabolic processes co-occur in brown adipocytes (Jung et al., 2021). If GE simultaneously stimulates *de novo lipogenesis* and glucose utilization in metabolically active adipocytes or if improved insulin-sensitivity in other adipocyte types promotes subcutaneous lipid storage remains unclear. Likewise, we cannot rule out that GE upregulates GLUT1 in other tissues and

overexpression of GLUT1 in skeletal muscle was shown to induce insulin resistance (Buse et al., 1996), which in turn is not evident in our glucose clamp data. Apart from the proposed GLUT1-mediated action, our data does further not rule out alternative mechanisms including direct insulin-sensitizing effects, increased insulin-independent glucose uptake via GLUT4-PM redistribution or liver-mediated effects due reduced gluconeogenesis. A recent molecular docking study identified GE as potential glucokinase activator, which could additionally modulate hepatic glucose metabolism as suggested from our clamp experiment (Khan et al., 2022).

In conclusion, we could show that reverse pharmacology is a valuable tool to identify undescribed compounds with pharmacological qualities when their chronic human use and observed outcomes have been recorded in traditional medicines. To our knowledge, this is the first comprehensive study, which successfully completed the reverse pharmacology approach for diabetes therapy. Selected based on a statistical association between traditional treatment and outcome as well as the measured clinical efficacy of PNe, we identified GE glycosides as one active principle and we elucidated adipocyte GLUT1 regulation as one underlying mode of action. Additionally, the effects of GE are comparable to metformin and highlight future possibilities to counteract T2DM by augmenting glucose clearance in GLUT1-dependent manner.

Limitations

Our study is limited to the DIO mouse model due to regulatory constraints and only one dose adopted from dietary PN supplementation was tested to date. Despite known effects of PNe in diabetics and the study on human adipocytes presented here, the efficacy and proposed mode of action of GE glycosides remain to be investigated in humans, which requires an in-depth toxicological assessment of GE as well as dose-finding studies. A genetic mouse model with adipose-specific deletion of *Glut1* could further strengthen our proposed molecular mechanism of action via GLUT1-mediated glucose uptake. However, it can be expected that in such a model compensatory mechanism might impact systemic metabolism. Furthermore, our study does not resolve if the insulin-sensitizing effect of GE is a consequence of the reduced systemic glucose load or a distinct primary event. We could conclude that genkwanin glycosides confer some of the therapeutic effects of PNe, but we cannot exclude that other compounds contribute to the biological activity of PNe phenotype or influence GE glycoside action in an additive or synergistic effect. In line with this, we reiterate that our hypothesis is that GE is a metabolite originating from genkwanin 5-O- β -primeveroside and genkwanin 5-O- β -glucoside after oral intake and is found within trace amounts only in the PNe per se. Although the cleavage of O-glycosylated flavonoids by intestinal metabolism was previously described (Németh et al., 2003), this phenomenon on PN O-glycosides needs to be verified by additional studies.

Acknowledgements

We thank Manuel Klug and Myrtha Arnold for experimental assistance with the hyperinsulinemic-euglycemic clamps. CH was supported by an SNF and Innosuisse BRIDGE Proof of Concept Fellowship (40B1-0_191463). Funding for collection and conservation of *Phaleria nisidai* leaves was provided by PAIR and Antenna Foundation. The Institute of Pharmaceutical Sciences of Western

Switzerland of the University of Geneva (Prof. J-L. Wolfender) is thankful to the Swiss National Science Foundation for the support in the acquisition of the NMR 600 MHz (SNF R'Equip grant 316030_164095). The graphical abstract was created with Biorender.

Authors contribution

CH, JH, CW, EFQ, and JLW conceptualized the study and wrote the manuscript. CK, BG, LM and AR, wrote and revised the manuscript. CH designed, performed and analyzed *in vitro* and *in vivo* studies. CM assisted with glucose clamps. HD and VE contributed to *in vitro* experiments. LB and MB generated the hMADS data. AH analysed the immunofluorescence images. JH performed extraction, fractionation, and purification of PN extract under supervision of EFQ and JLW. LM performed NMR analyses. AR performed UHPLC-HRMS/MS analyses. CK, BG and VY represent the Republic of Palau, provided the genetic resources and shared traditional knowledge.

Declaration of interests

Authors declare no competing interests.

Figure legends

Figure 1: PNe alleviates glucose homeostasis in DIO mice.

(A) Schematic outlay of the dietary intervention (DI).

(B) Body weight development during DI as percentage of start weight.

(C) Final body weight after 7 weeks of DI.

(D) Body composition after 5 weeks of DI.

(E-F) (E) Insulin tolerance test and (F) corresponding AUC after 12 weeks HFD and 5 weeks DI. n=6

(G-J) Fasting (G) insulin, (H) triglyceride, (I) NEFA and (J) cholesterol concentrations after 12 weeks HFD and 7 weeks DI. n=5-8 per group

(K-L) (K) Oral glucose tolerance test and (L) corresponding AUC after 6 weeks HFD and 2 weeks DI. n=7-8 per group.

(M) Plasma insulin levels 30 min after an oral glucose load after 6 weeks HFD and 7 weeks DI. n=6-7 per group

(N) Urinary glucose concentration after 6 weeks HFD and 6 weeks DI. n=9-12 per group.

(O-P) (O) Blood glucose concentrations over time after an acute oral dose of PNe (130 mg/kg BW) vs vehicle after 10 days of HFD and (P) reduction in blood glucose levels from time point 240 mins vs baseline. n=9 per group. (Q-V) Tissue specific ¹⁴C-2-deoxyglucose glucose uptake into (Q) gastrocnemius, (R) soleus, (S) liver, (T) iWAT, (U) iBAT and (V) eWAT after 6 weeks HFD and 7 weeks DI. n=6 per group.

Results are reported as mean ± SEM. Two-tailed student's t-test for comparisons between two groups was applied in C, F-J, L, N, P-V. 2-way (D) or 2-way repeated measures ANOVA was applied in B-E, K, M and O with Sidak's post-hoc comparison. Statistical differences are indicated as *p<0.05, **p<0.01, ***p<0.001.

Figure 2: PNe increases adipocyte glucose uptake via insulin-independent GLUT1 *in vitro*.

(A) Color coding of bar graphs displayed in figures 2 and 3. 200 µg/mL of PN was applied for 3 days in all experiments.

(B-C) Glucose uptake in basal and insulin-stimulated (100 nM, 60 min) condition in (B) 3T3-L1 and (C) brown adipocytes. (n=10-12)

(D-H) (D) Western blots for GLUT1 and GLUT4 in both adipocyte cell lines and (E-H) quantification. (n=6).

(I-M) (I) Western blots for AKT^{pS473} and AKT^{pT308} with or without insulin stimulation (20 min, 10 nM) in both adipocyte cell lines and (J-M) quantification. (n=6)

(N-O) Glycolytic stress test in (N) 3T3-L1 and (O) brown adipocytes. (n=11)

(P-Q) ³H-Glycolytic flux analysis of (P) 3T3-L1 and (Q) brown adipocytes. (n=8-12)

(R-S) Gene expression analysis of targets regulating glucose metabolism in (R) 3T3-L1 and (R) brown adipocytes. (n=9-14)

(T-V) (T) Western blots of glucose transporters in iWAT and BAT from mice after 12 weeks of DI and (U-V) quantification. (n=5-6)

(W-Y) Western blots of glucose transporter proteins in human brown and white hMADS and quantification of (X) GLUT1 and (Y) GLUT4. (n=3)

Results are reported as mean ± SEM. Two-tailed student's t-test for comparisons between two groups was applied in P-Q, Multiple t-test with Holm-Sidak post-hoc test was applied in B-C, E-H, J-M, R-S, U-V and X-Y. 2-way ANOVA with Dunnett's post-hoc test was applied in N-O. All comparisons were performed against untreated control cells. Statistical differences are indicated as *p<0.05, **p<0.01, ***p<0.001.

Figure 3: Short-term PNe activates the PKC-ERK1/2 axis.

(A-B) Glucose uptake in (A) 3T3-L1 and (B) brown adipocytes after acute PNe (colored bar) treatment (200 µg/mL, 3 hours). n=8-9 per group.

(C-G) (C) Western blots for AKT^{pS473} and AKT^{pT308} in both adipocyte cell lines with or without insulin stimulation (10 nM, 20 min) and (D-G) quantification. n=6 per group.

(H) Pan phosphoPKC substrates antibody with PMA (250 nM) as positive control.

(I-L) Time course of GLUT1 phosphorylation at S226 following PNe treatment in (I) 3T3-L1 and (J) brown adipocytes and (K-L) quantification.

(M) Effect of PKC inhibition with Gö-6893 (30 min, 1 µM) on GLUT1^{pS226} levels following 3 hours of PNe stimulation.

(N) Glucose uptake assay with pretreatment of the PKC-inhibitor Gö-6893 (30 min, 1 µM) in 3T3-L1 and brown adipocytes. n=8 per group.

(O-P) (O) ERK1/2 phosphorylation at Thr204 and Tyr202 following PNe stimulation in brown adipocytes and (P) quantification of ERK^{pThr202/pTyr204}. n=6 per group.

(Q) *Glut1* mRNA levels in response to PNe exposure (4 hours) with or without pretreatment with the ERK1/2 inhibitor PD184352, 500 nM, 30 min). n=11-12 per group.

(R-S) (R) Quantification of ERK1/2 localization after PNe or PMA treatment (180 min) with or without PKC-inhibitor Gö-6893 (250 nM). (n=5-6 images per condition from 3 replicates with 200-250 cells per image). (S) Representative immunofluorescence pictures stained for nuclei (blue) and ERK1/2 (green) used for quantification in (R). Scale bar 100 µM.

(T) Glucose uptake after 16 hours of PNe with or without pretreatment by ERK1/2 inhibitor PD-98059 (500 nM, 30 min) in brown adipocytes. n=5-6 per group.

Results are reported as mean \pm SEM. Multiple student's t-test with Sidak's post-hoc test was applied in A-B and D-G. One-way ANOVA with Dunnett's post-hoc test was applied in K-L and Q. One-way or two-way ANOVA with comparisons between all groups and Tukey's post-hoc test was applied in O, R-S and U. Statistical differences are indicated as * $p < 0.05$, ** $p < 0.01$, *** $p < 0.001$.

Figure 4: Bioactivity-guided fractionation of PNe reveals F4 as source of bioactive substances.

(A) Experimental set up of the dietary intervention (DI) and applied doses.

(B) Random fed blood glucose measured at 11 am. n=6-8 per group.

(C-F) (C) Insulin tolerance test and (D) AUC after 4 weeks of DI. (E) Insulin tolerance test after 10 weeks DI and (F) AUC. n=6-7 per group.

(G-H) (G) Oral glucose tolerance test (2g/kg BW) after 11 weeks DI and (H) AUC. n=6-8 per group.

(I) Circulating active GLP-1 levels 2 mins after an oral glucose load. n=6-7 per group.

(J) Fasting blood glucose concentrations at the end of the DI.

(K) Experimental set up of the DI with metformin (MET) as positive control drug. n=7-9 per group.

(L) Glucose infusion rates (GIR) at steady state during hyperinsulinemic-euglycemic clamps. n=7-9 per group.

(M) Basal and insulin-stimulated whole-body glucose turnover. n=7-9 per group.

(N) Endogenous glucose production (EGP) during basal and insulin-stimulated conditions. n=7-9 per group.

(O-T) Tissue-specific ^{14}C -2-deoxyglucose uptake rates into the (O) eWAT, (P) iWAT, (Q) iBAT, (R) liver, (S) soleus and (T) gastrocnemius. n=6-9 per group.

Results are reported as mean \pm SEM. One-way ANOVA with Dunnett (D, F, H, I, J) or Holm-Sidak's post-hoc (L, P-U) tests were applied for comparisons against HFD controls. Two-way ANOVA with Dunnett's post hoc test was applied in B-C, E, G and N-O. Statistical differences are indicated as * $p < 0.05$, ** $p < 0.01$.

Figure 5: GE glycosides mediate the beneficial effects of F4.

(A) Structures of flavones tested *in vivo*, among which GP, GG and IX were isolated in F4, while GE and AP were selected as potential metabolites biotransformed in the digestive system after ingestion of the aforementioned constituents of F4.

(B) Experimental set up and applied doses during the DI.

(C-D) (C) Insulin tolerance test after 7 weeks of DI and (D) AUC. n=18-20 per group

(E-F) (E) Glucose tolerance test after 8 weeks of DI and (F) AUC. n=20 per group

(G) Random fed blood glucose concentrations after 9 weeks of DI. n=8-10 per group.

(H) Fasting urinary glucose concentrations after 4 weeks of DI. n=7-10

(I) Ratio of visceral (VAT) to subcutaneous (SAT). n=8-10 per group.

Results are reported as mean \pm SEM. Two-way ANOVA with Dunnett's post-hoc test was applied in C and D. One-way ANOVA with Dunnett's post-hoc test was applied in D and F-I. All comparisons were performed against HFD controls. Statistical differences are indicated as * p <0.05, ** p <0.01, *** p <0.001.

Figure 6: GE supports insulin action by promoting basal glucose uptake.

(A-C) ^{14}C -2-deoxyglucose uptake into (A) iBAT, (B) iWAT and (C) eWAT after 6 weeks HFD and 6 weeks DI. n=9-10 per group

(D-G) Effect of GE on (D-E) GLUT1 protein and (F-G) GLUT1 phosphorylation at S226 in the iBAT (brown bar) and iWAT (white bar). n=9-10 per group.

(H-I) Effect of GE on GLUT4 protein in the (H) iBAT and (I) iWAT. n=9-10 per group.

(J-M) Effect of GE on (J-K) AKT phosphorylation at S473 and (L-M) total AKT levels in iBAT (brown bars) and iWAT (white bars). n=9-10 per group.

(N-Q) Western blots quantified in D-M from (N-O) BAT and (P-Q) iWAT of random fed animals after 9 weeks DI. n=9-10 per group.

Results are reported as mean \pm SEM. Two-tailed student's test was applied in all comparisons. Statistical differences are indicated as * p <0.05, ** p <0.01.

Figure 7: GE competes against metformin in hyperinsulinemic-euglycemic clamps.

(A) Experimental set up for hyperinsulinemic-euglycemic clamps.

(B and C) (B) Glucose infusion rate (GIR) over the course of the clamps and (C) GIR during the steady state condition. n=7-9 per group.

(D) Blood glucose concentration during the clamp procedure. n=7-9 per group

(E) Insulin-stimulated glucose disappearance rate (IS-GIR) at steady state condition. n=7-9 per group

(F and G) (F) Whole body glucose turnover and (G) endogenous glucose production (EGP) during basal and insulin-stimulated states. n=7-9 per group.

(H-M) ^{14}C -2-deoxyglucose uptake into (H) eWAT, (I) iWAT, (J) iBAT, (K) liver, (L) soleus and (M) gastrocnemius after 35 min into steady state. n=7-9 per group

Results are reported as mean \pm SEM. One-way ANOVA with Dunnett's post-hoc test was applied in figures C, E and H-M. Two-way ANOVA with Dunnett's post-hoc test was applied in figures B, F and

G. All comparisons were performed against HFD controls. Statistical differences are indicated as * $p < 0.05$, ** $p < 0.01$, *** $p < 0.001$.

Methods

Resource Availability

Lead Contacts

Further information and requests for resources and reagents should be directed to and will be fulfilled by the Lead Contact, Christian Wolfrum (christian-wolfrum@ethz.ch). Questions related to phytochemical profiling, fractionation and extract preparation should be addressed to Lead Contact, Jean-Luc Wolfender (Jean-Luc.Wolfender@unige.ch).

Materials Availability

This study did not generate new unique reagents.

Data and Code Availability

All data related to bioactivity reported in this paper will be shared by the Lead Contacts on request.

Bio guided fractionation data have been deposited in the YARETA repository and have the following DOI: <https://doi.org/10.26037/yareta:2j2b4d5ivjeudbcsbxmxcpgjq>. This data includes the chemical profiling of PNe and its four fractions obtained by UHPLC-PDA-HRMS/MS, the chemical profiling of fractions F2 and F4 obtained by UHPLC-PDA-QDA-MS-ELSD, and NMR spectra of the four fractions and all isolated constituents. During the submission process: please contact the corresponding author for data access.

No code was generated as part of the study.

Experimental models

Mouse models

All animal experiments were approved by the Veterinary Office of the Canton of Zürich, Switzerland. Male C57B6N mice were obtained from in house breeding or purchased from Charles River laboratories. Experimental mice were housed in groups of 2-4 animals in individually ventilated cages with a reversed 12-hours dark/light cycle (lights on 7 pm) at a housing temperature of 23°C. Mice had *ad libitum* access to standard laboratory chow diet (18 % proteins, 4.5 % fibers, 4.5 % fat, 6.3 % ashes, Provimi Kliba SA) and water. Diet was switched to high fat diet (23.9 % proteins, 4.9 % fibers, 35 % fat, 5.0 % ashes, Provimi Kliba SA) at age of 6-7 weeks. Dietary intervention started after 6-12 weeks of initial HFD-feeding depending on the experiment as indicated in the figure legends. The health state of the mice was regularly checked according to FELASA guidelines and food intake measured at the beginning of the DI to exclude potential food aversion.

Dietary supplementation

Animal diets supplemented with PN, F2, F3, F4, isolated compounds or metformin were produced in house from powdered high fat diet with the same composition as above (Provimi Kliba SA). Metformin was added at a dose of 0.25% and has previously shown to be effective (Matsui et al., 2010). For the concentrations of compounds and fractions see section "Fraction preparation and dosage for *in vivo* testing". The required amounts of supplements were calculated based on a daily food intake of 3 g per mouse. The PN extract and fractions were first dissolved in H₂O and then mixed with the HFD powder (20 mL H₂O per 100 g HFD) using an electronic kitchen machine. The right amounts of single individual compounds were dissolved in DMSO (final DMSO concentration in food 0.001%) small droplets of human grade food colorant (Betty Bossi, Coop) were added and dough mixed until homogenous. Pellets were formed by hand, dried overnight and stored at 4°C. Food was prepared every 10 days to ensure stability of the compounds.

Cell culture – immortalized brown adipocytes

This cell line was kindly provided by Prof. Klein (Klein et al., 2002) and produced from stromal-vascular fraction isolated brown preadipocytes of the iBAT of male and female C57BJ mice by immortalization with the SV40 antigen. Cells were used at passages 4-10. Preadipocytes were cultured in complete media consisting of high glucose DMEM supplemented with 10% heat-inactivated FBS (Gibco) and 1% Pen/Strep (Gibco) in a normoxic, humidified cell culture incubator (37°C, 5% CO₂). Brown preadipocytes were grown on collagen-I (1:500) coated p10 plates and grown until confluency. Post-confluent cells were induced for differentiation into adipocytes with an induction cocktail containing insulin (20 nM), IBMX (500 µM), dexamethasone (1 µM) and T3 (1 nM) in complete media. 2-days post-induction, media was replaced by maintenance media with insulin (20 nM) insulin and T3 (1nM) and this media was exchanged every other day. At day 5 of differentiation, cells were trypsinized and replated on 24- or 12-well dishes for experiments at a density of 400'000 cells/mL. Long-term treatments with PN were performed on three subsequent days (d6, d7, d8). PN was directly dissolved into the media at the indicated concentrations and the solution freshly prepared before use every day. Cells were harvested or experiments performed on day 9 of differentiation. Short-term PN stimulation was performed at day 9 of differentiation in serum-free media.

Cell culture – 3T3-L1 adipocytes

3T3-L1 fibroblasts are a subclone of the 3T3-Swiss albino cell line, which was generated from murine embryonic tissue by spontaneous clonal immortalization (Todaro and Green, 1963). 3T3-L1 fibroblasts were obtained from the ATCC whereas the original passage of this cell line is unknown we used the cells up to 11 passages. 3T3-L1 fibroblasts were cultured in complete media consisting of high glucose DMEM supplemented with 10% heat-inactivated FBS (Gibco) and 1% Pen/Strep (Gibco) in a normoxic, humidified cell culture incubator (37°C, 5% CO₂). 3-days post-confluent 3T3-L1 cells grown on collagen-I coated (1:500) p10 dishes were induced for 48 hours with an induction cocktail containing insulin (170 nM), IBMX (500 µM), rosiglitazone (and dexamethasone (1 µM). Media was replaced with insulin media (170 nM) for another 2 days and cells were subsequently maintained in standard DMEM without

additives and media changed every second day. Treatments and replating were performed as outlined above under “immortalized brown adipocytes”.

Cell culture – hMADS

Human multipotent adipose-derived stem (hMADS) cells originating from the prepubic fat pad of a 4-month-old male were kindly provided by Dr. Amri and cultured as previously described (Balaz et al., 2019; Elabd et al., 2009). Briefly, cells (passage 15) were grown in low glucose DMEM supplemented with 15mM HEPES, 10% FBS, 2mM L-glutamine, 1% Penicillin/Streptomycin and 2.5ng/ml recombinant human FGF-2 in normoxic humidified cell culture incubator (5% CO₂ and 37°C). Differentiation of 48 hours post-confluent cells was induced (day 0) by adipogenic medium (DMEM/Ham’s F12 media containing 10µg/ml Transferrin, 10nM insulin and 0.2nM triiodothyronine) supplemented with 1µM dexamethasone and 500µM isobutyl-methylxanthine (IBMX) From day 2 to 9, cells were cultured in adipogenic medium containing 100nM rosiglitazone and medium was refreshed every 2 – 3 days. Cells were kept in culture until day 18 in absence of rosiglitazone to obtain mature white adipocytes. To obtain brown adipocytes, cells were exposed to an additional rosiglitazone pulse between days 14 - 17. To investigate the effect of the plant extract on white and brown adipocyte functionality and GLUT1 levels, cells were exposed to different concentrations of the extract (1.6 - 200µg/ml) between day 14 and 17. Fresh medium was provided every 24 hours. Adipocytes were cultured until day 17, when cellular respiration was determined, or cells were harvested for protein analysis.

Methods details

Tissue harvest

Animals were euthanized individually with a CO₂ overdose and blood collected by cardiac puncture with EDTA (0.5 M) flushed syringes. Whole blood was spun for 20 min at 2000 g and blood plasma stored at -80°C until downstream analysis. Tissues were carefully dissected, snap frozen in liquid nitrogen and stored at -80°C for protein extraction. For tissue specific glucose uptake measurements and glucose clamps studies, the animals were euthanized by cervical dislocation.

Body composition

Lean and fat mass of alive mice were determined with a magnetic resonance imaging system (EchoMRI 130, Echo Medical Systems). Data were calculated by the EchoMRI 14 Software.

Cumulative food intake

Phenomaster metabolic cage system (TSE system) was used to measure cumulative food intake (Figure S5B). Mice were held individually and adopted to the single caging for 2 days before measurements started.

Intraperitoneal insulin tolerance test

Mice were fasted for 6 hours at the beginning of the active phase. An intraperitoneal dose of insulin (0.75-1,2 U/kg BW, Actrapid human insulin, Novo Nordisk) was injected after recording of fasting blood glucose concentration (ACCU-CHEK Aviva, Roche) through a small incision in the tail. Blood glucose concentrations were monitored for 2 hours, and blood samples measured at 0, 15, 30, 60, 90 and 120 minutes.

Oral and intraperitoneal glucose tolerance test

Mice were fasted for 6 hours at the beginning of the active phase. An intraperitoneal or oral dose of glucose (2 g/kg BW) was administered after recording (Accu-Check, Roche) of fasting blood glucose concentration (Accu-Check, Roche) through a small incision in the tail. Blood glucose concentrations were monitored for 2 hours, and blood samples measured at 0, 15, 30, 60, 90 and 120 minutes.

Glucose-stimulated insulin secretion

Mice were fasted for 6 hours at the beginning of the active phase. A blood sample was collected with a glass capillary from the tail to determine fasting blood glucose levels. An oral dose of glucose (2 g/kg BW) was administered via gavage and 15 min later a second blood sample collected to determine glucose-stimulated insulin levels. Blood samples were centrifuged for 8 min at 8000g, and plasma collected. Insulin concentrations were determined with the MesoScale Discovery kit.

GLP-1 measurement

Mice were fasted for 6 hours and were orally given 200 μ L of 20% glucose solution. 2 minutes later, a blood sample was collected from the tail vein with a micro cuvette, and DPPV-4 inhibitors added. Whole blood was spun at 4°C at 8000 g for 8 min to collect the plasma. Circulating, active GLP-1 levels were measured with the active GLP-1 MesoScale Discovery Elisa Kit.

Urinary glucose extraction

Urine was collected after 6 hours of food deprivation at the beginning of the light cycle by mildly restraining the mouse and massaging the bladder. Urine was stored at -80°C until glucose concentrations were determined using a colorimetric glucose assay kit (MAK263-1KT, Sigma).

Metabolic blood parameters

The following commercially available kits were used determine triglycerides (11877771 216, Roche/Hitachi), ultrasensitive mouse Insulin Elisa Kit (90080, Crystal Chem), non-esterified fatty acids (436-91995 and 434-91795, FUJIFILM Wako Chemicals), cholesterol (11491458 216, Roche/Hitachi) or ALT activity assay (MAK052-1KT, Sigma) in blood plasma samples according to the manufacture's guidelines.

Tissue-specific glucose uptake

Animals underwent an initial HFD-feeding period of 6 weeks and glucose uptake was assessed after 6-7 weeks of dietary intervention with PN or GE. were fasted for 6 hours at the beginning of the dark cycle. 100 μ L of were injected via the tail vein and animals were sacrificed after 30 min by cervical

dislocation, tissues harvested and snap frozen in liquid nitrogen. To determine tissue-specific glucose uptake, the tissue was lysed in 2mL of H₂O and homogenized using a tissue homogeniser from POLYTRON. Phosphorylated ¹⁴C-2-deoxyglucose was isolated from the tissue lysate using chromatographic columns (7316212, BioRad). 1 mL of lysate was incubated in 5 mL of liquid scintillation fluid (Ultima Gold) overnight and counted with a Perkin Elmer TriCarb 2000 CABeta-Counter for 5 mins per sample. DPM were normalized to initial tissue weight.

Hyperinsulinemic-euglycemic clamps

Animals underwent an initial HFD-feeding period of 6 weeks followed by 7-8 weeks of dietary intervention with F4 or GE. Hyperinsulinemic-euglycemic clamps were performed as previously described in (Grandl et al., 2018; Wueest et al., 2010). A polyurethane catheter was inserted into the left jugular vein and exteriorized at the next region under isoflurane anesthesia. Prior to surgery, Vitamin A salve was applied onto the eyes and the analgesic fentanyl (50 µg/kg bodyweight) was administered. The catheters were filled with heparinized-glycerol solution. A single subcutaneous dose of norocarp was given 16 hours post-surgery. Body weight and health state were monitored daily. Animals with less than 10% loss of preoperative weight were included in the subsequent clamps and animals could recover for at least four days. Animals were starved for 6 hours prior to clamping. Catheters were flushed with 0.9% NaCl and mice placed into restrainers, which allowed them to move freely. Basal glucose production was measured for 80 minutes with a continuous ³H-glucose infusion. The clamps were performed with the HARVARD apparatus and insulin (Actrapid Human Insulin, Novo Nordisk) infusion rate was set to 12 mU/kg⁻¹*min⁻¹. Glucose was infused at a variable rate and target blood glucose concentration set to 6 mM. Blood glucose levels were monitored every 5 or 2.5 minutes with a glucometer (Akku-Check Aviva, Roche) and infusion rates adjusted accordingly. Steady state glucose infusion rate was recorded when the glucose infusion rate remained constant with only minor deviations for 15-20 min at a blood glucose concentration of 6 mM. Once steady state conditions were reached, a single bolus of ¹⁴C-2-deoxyglucose was administered through the catheter to determine tissue-specific glucose uptake rates over 35 minutes. Blood samples were collected at times=0 (bolus), 2-, 15-, 25- and 35-minutes post injection. Mice were sacrificed by cervical dislocation and the following tissues collected for analysis: iWAT, eWAT, soleus, gastrocnemius, BAT and liver. The area under the curve of the disappearing plasma ¹⁴C-2-deoxyglucose was combined with the tissue counts of phosphorylated ¹⁴C-2-deoxyglucose to calculate tissue specific glucose uptake rates. Tissue samples were weighed and homogenized as above under "Tissue-specific glucose uptake". Phosphorylated 2-deoxyglucose was isolated using chromatographic columns (7316212, BioRad)(Chin et al., 2015) and 1 mL of lysate counted in 5 mL of liquid scintillation cocktail (Ultima Gold) for 5 min with the Perkin Elmer TriCarb 2000 CABeta-Counter after overnight incubation.

mRNA isolation and qPCR

mRNA was isolated with TRIzol reagent (Invitrogen) according to the manufacture's instruction. A 30 min DNase treatment was included to remove genomic DNA (NEB BioLabs). 1000 ng of total RNA was reverse transcribed into cDNA using the High Capacity Reverse Transcription kit (Applied Biosystems).

cDNA was diluted to 5ng/μL with ddH₂O. Quantitative RT-PCR was performed with Fast SYBR green (Applied Biosystems) on a 384-well format Viia 7 machine (Applied Biosystems). qPCR Primers were designed with the online NCBI primer design tool and synthesized by Microsynth. Relative mRNA expression was calculated by the delta-delta Ct method. TBP served as housekeeping genes. All qPCR primer sequences are listed in Table S2.

Protein extraction and western blot analysis

Whole cell protein was extracted from adipose depots and cell cultures using RIPA Buffer (50mM Tris-HCl pH 7.4, 150mM NaCl, 2mM EDTA, 1.0% Triton X100, 0.5% sodium deoxycholate and 10% glycerol for adipose tissue) supplemented with protease (Complete, Roche) and phosphatase inhibitors (Haltphosphatase inhibitor cocktail, ThermoFisher). The lysate was spun at 12'000 g for 15 min at 4°C and the supernatant carefully collected. Protein concentrations were determined with the DC Protein Assay (Bio-Rad). For Western Blotting, equal amounts of proteins were loaded onto 12% or 8% SDS-Polyacrylamide gels and transferred on nitrocellulose (Bio-Rad) membranes. Membranes were blocked for 1 hour at RT with either 5% BSA or 5% fat free milk depending on the antibody. The following primary antibody bodies were used and incubated overnight at 4°C GLUT4 (1:1000, Merck 07-1404), GLUT1 (1:1000, Merck 07-1401), GLUT1^{pS226} (1:200, Merck ABN991), AKT (1:0000, Cell Signaling 9272), AKT^{pS473} (1:1000, Cell Signaling 4060), AKT^{pT308} (Cell Signaling 13038), ERK1/2 (1:1000, Cell Signaling 4695), ERK1/2^{pThr202/Tyr204} (1:1000, Cell Signaling 4370), HSP90 (1:1000, Cell Signaling 4877), GADPH (1:1000, Cell Signaling 5174), phosphoPKC Substrates (1:1000, Cell Signaling 2261), PPARγ (1:1000, Cell Signaling 2443). The HRP-conjugated secondary antibody (1:10'000 Cell Signaling) signal was detected with the Image Quant system (GE Healthcare Life Sciences).

Glucose uptake assay

Glucose uptake assays were done in 24-well plates as described elsewhere (Beaton et al., 2015) after 1 hour of insulin stimulation. In brief, cells were serum-starved for 3 hours in the presence or absence of the specified stimuli. ERK1/2 inhibitor (PD98095) or PKC inhibitor (Gö-6893) were added 30 min before end of starvation. Insulin (Actrapid Human Insulin, Novo Nordisk) was added to a final concentration of 100 nM and cells stimulated for 50 min. Plates were carefully washed 2x with Krebs-Ringer-Hepes (KRH) Buffer (50mM HEPES, 137mM NaCl, 4.7mM KCl, 1.85mM CaCl₂, 1.3 mM MgSO₄, pH 7.4) with 0.1% fatty acid free BSA to remove any extracellular glucose. Cells were then incubated at 37°C with 0.1 μCi ¹⁴C-2-Deoxyglucose in 200 μL of KRH Buffer. The uptake reaction was stopped with 4 thorough, ice-cold PBS washes. Cells were lysed in 0.1 M NaOH, and lysate transferred to 2 mL of liquid scintillation cocktail. 10 μL of cell lysate was kept aside for protein determination. Radioactive decays were counted with a Perkin Elmer TriCarb Beta-Counter for 2 minutes.

Glycolytic stress test

Preadipocytes were grown and differentiated on p10 plates until day5 of differentiation. Differentiating adipocytes were collected by trypsinization and replated at a density of 7000 cells per well. The cells were treated daily for 72 hours. On the day of the assay, cells were washed 3x with PBS and incubated for one hour in the Seahorse XF Base Medium (Agilent, 102353-100) supplemented with 2mM

glutamine (GlutaMAX, Gibco 35050-061). Oxygen consumption rates and extracellular acidification rates of the media were measured with extracellular flux analyzer (Seahorse XFe96, Agilent Technologies). After baseline measurements were acquired, the following compounds were successively injected into the media a) glucose (10 mM final) b) oligomycin (1 μ M final) c) 2-deoxyglucose (100 mM final). Three measurements were performed after each injection within 3 minutes intervals. Read out were normalized to protein content per well. Glycolysis, glycolytic capacity and spare capacity were calculated from the normalized values according to the manufacture's guidelines.

Glycolytic flux analysis

Glycolytic flux was measured in mature adipocytes after 3 days of PN treatment as described in (Veys et al., 2019) In short, cells were starved with or without PN in KRH (see above) for 2 hours and then incubated with labelling media (high glucose DMEM, 0.4 μ Ci/mL of 3 H-5-glucose) and cells incubate for 2 hours at 37°C. Empty wells were used to determine the background signal. Meanwhile, hanging wells were inserted into rubber stoppers and a piece of filter paper (1x6 cm) was placed in each hanging well. At the end of the incubation period, the filter paper was hydrated with 200 μ L of ddH₂O. 200 μ L of labelling media were then transferred to glass vials and 50 μ L of 3 M perchloric acid were added to prevent any further metabolic activity from potentially transferred cells. The glass vials were tightly closed with the rubber stoppers containing the hanging wells and incubated for 48 hours at 37°C. Each filter paper was then carefully transferred into scintillation vials containing 5 mL of liquid scintillation cocktail. The samples were left at room temperature overnight and subjected to liquid scintillation counting (2 min per vial, Perkin Elmer TriCarb). Glycolytic flux was calculated as pmol glucose per hour and normalized to protein content.

Immunofluorescence

Differentiating adipocytes were replated at day5 of differentiation into glass-bottom 96-well plates at a density of 35'000 cells. Cells were washed 2x with PBS, fixed (4% formaldehyde, 20 min at 4°C) and washed again 3x with PBS. Blocking (3% BSA) and permeabilization (0.1% Triton X-100) were performed at room temperature for 1 hours or 10 min, respectively. Primary anti-ERK1/2 antibody (1:500, Cell Signaling 4695) was incubated overnight at 4°C. After extensive washing, alexa488-conjugated secondary antibody (1:750, Life Technologies A21206) was applied for 1 hour at RT. Nuclei were stained with Hoechst (1:10'000, Cell Signaling 4082) in PBS for 10 min. Images were acquired with the automated Operetta microscope (Perkin Elmer). The representative images are cropped section from original images to provide better resolution. The acquired images were analyzed to determine the percentage of cells positive for on overlap between nuclear Hoechst (nuclei) and alexa488 staining (ERK1/2). Nuclear alexa488 staining was estimated by the ratio between average alexa488 signal within the nuclear area and the average signal intensity around the nuclear envelope in a ~3 pixels wide ring. The image processing was performed with custom scripts developed in MATLAB 2019a.

Quantification and statistical analysis

Data are presented as mean \pm SEM for all graphs. Statistical analysis was performed using GraphPad prism. Sample sizes were selected based on previous experience and findings for a certain method. The authors were not blinded during the procedures or data analysis. The statistical method and n-number for each experiment is indicated in each figure legend. *In vitro* experiments with murine cell lines were performed with 3 technical replicates for protein, 4-6 replicates for radioactive assays and 6 replicates for RNA isolation and each experiment was independently reproduced 2-3 times. Proof of concept experiments with hMADS were performed once. Unless stated differently, the following tests were applied: unpaired, two-tailed student's t-test was performed when two groups were compared. If multiple treatments were analyzed, one-way ANOVA was performed in comparison to control (untreated cells) with Dunnett's multiple comparisons test. In experiments with multiple variables, repeated measures (tolerance tests, random fed blood glucose) or ordinary two-way ANOVA with Dunnett's multiple comparisons test was used. $p < 0.05$ was considered as statistically significant.

Preparation of *Phaleria nishidai* leaf extract

The leaves of *Phaleria nishidai* Kaneh. (Thymelaeaceae) were collected at the time of the clinical study (Kitalong et al., 2017) and reference specimens were deposited at the Belau National Museum Herbarium. The leaves of PN were extracted by decoction according to the traditional recipe used by the population of Palau (Kulakowski et al., 2015). The dried leaves were extracted by decoction for 1 hour, then freeze-dried to facilitate mouse feeding and chemical investigation. The decoction was performed without a lid to evaporate potentially irritating compounds since the leaves have been reported to contain toxic volatile compounds removed upon boiling (Kulakowski et al., 2015). After filtration ($60^{\circ}\text{C} \pm 5^{\circ}\text{C}$) and first evaporation with rotavapor to reduce the water quantity (Büchi SARL, Rungis, France), the decoction was freeze-dried (-80°C , 0.01 bar, Christ Alpha 2-4 LD plus, Osterode am Harz, Germany) and stored at 4°C . For the complete study, 200 g of dried leaves were extracted in two batches of 100 g, in portions of 30 to 40 g, which required a total of 20 L of water. In the two batches, the yield of extraction was $28.6\% \pm 0.7\%$ (average \pm standard deviation, $n=7$) (w/w). The volume of water lost by evaporation during the decoction was measured at 1.4 L (± 0.0 L, $n=3$), independent of the initial volumes (respectively at 4.0 L and twice 3.0 L).

Chemical profiling

Chemical profiling was acquired on two independent UHPLC systems, one equipped with photo diode array (PDA) and Charged Aerosol Detector (CAD) (UHPLC-PDA-CAD), and the second with PDA and high-resolution mass spectrometer (UHPLC-PDA-HRMS/MS), to obtain qualitative (UV and HRMS/MS spectra) and semi-quantitative (CAD) information. The chromatographic conditions were the same for both systems: samples were injected (2 μL) into an Acquity UPLC BEH C18 column (2.1 x 150 mm i.d., 1.7 μm , Waters, Milford, MA, USA) and eluted (0.4 mL/min, column temperature set at 40°C) with water (A) and acetonitrile (B) both containing 0.1% formic acid with the following gradient: from 5 to 50% of B from 0 to 25 min (curve 7), 50 to 95% of B from 25 to 30 min, an isocratic step at 95 % for 5 minutes and a re-equilibration step of 5 min. Semi-quantitative profiling (UHPLC-PDA-CAD) were acquired with a Vanquish system (Thermo Fisher Scientific, Waltham, MA, USA), which was equipped with an UHPLC hyphenated with a PDA (HL-type) and a CAD (VF-D20A type) (set at 35°C , data collection rate at 10Hz),

controlled by the software Chromeleon 7.2.9. HRMS/MS chemical profiling were performed on an Acquity UPLC system interfaced to an Orbitrap Q-Exactive Focus mass spectrometer (Thermo Scientific), using a heated electrospray ionization (HESI-II) source. Xcalibur 2.1 software (Thermo Scientific) was employed for instrument control. An Acquity UPLC PDA detector acquired the UV trace from 200 to 500 nm. The full MS analyses were performed in positive mode with a mass range of 150-1500 at a resolution of 35000 full width at half maximum (FWHM) (at m/z 200). In positive mode, diisooctyl phthalate C₂₄H₃₈O₄ [M+H]⁺ ion (m/z 391.28429) was used as internal lock mass. The optimized HESI-II parameters were the following: source voltage: 3.5 kV (pos); sheath gas flow rate (N₂): 50 units, auxiliary gas flow rate: 12.50 units, spare gas flow rate: 2.5; capillary temperature: 262.5°C; S-Lens RF Level: 45. The mass analyzer was calibrated according to the manufacturer's directions using a mixture of caffeine, methionine-arginine-phenylalanine-alanine-acetate (MRFA), sodium dodecyl sulfate, sodium taurocholate and Ultramark 1621 in an acetonitrile/methanol/water solution containing 1% acetic acid by direct injection. The data dependent HRMS/MS events were performed on the three most intense ions detected in full scan MS (Top3 experiment). The HRMS/MS isolation window width was 1 m/z and the normalized collision energy (NCE) was 35 units. In data dependent HRMS/MS experiment, full scans were acquired at a resolution of 35000 FWHM (at m/z 200) and HRMS/MS scans at a resolution of 17 500 FWHM with a maximum injection time of 50 ms. After being acquired in HRMS/MS scan, parent ions were placed in a dynamic exclusion list for 2.0 second.

The samples whose chemical profiling were acquired were solubilized in a solution of water and methanol (70/30 v/v). The freeze-dried decoction of PN and the fractions had a concentration of 2 mg/mL, while precipitated MG was prepared at 250 mg/mL. After sonication (10 min), samples were centrifugated (13'000 rpm, 10 min) (Prism R, Labnet international Inc., Edison, NJ, USA).

Mangiferin quantification in PN extract

Mangiferin (MG) in PNe was quantified by external quantification at the UV wavelength of 256 nm on the UHPLC-PDA system described in the section above. The chromatographic conditions were as followed: PN extract and calibrations were injected (1 μ L) into an Acquity UPLC BEH C18 column (2.1 x 100 mm, i.d. 1.7 μ m, Waters, Milford, MA, USA) and eluted (0.4 mL/min, column temperature set at 40°C) with water (A) and acetonitrile (B) both containing 0.1% formic acid with the following gradient: from 5 to 50% of B from 0 to 8 min (curve 7), 50 to 95% of B from 8 to 9 min (curve 6), an isocratic step at 95 % for 2 minutes and a re-equilibration step of 1.9 min. The PNe was solubilized at 1 mg/mL in a solution of water and methanol (8/2 v/v) and sonicated 10 min. Four calibration solutions were prepared with MG standard from 50 to 400 μ g/mL in the same solution than PN extract. The calibration curve was: $y = 178.02x - 1001.4$ and R^2 of 0.999. The MG concentration measured in PNe was of $14.5 \pm 0.4\%$ (n=4).

Large scale fractionation of PNe to obtain fractions with complementary compositions for *in vivo* studies

To remove the polar compounds that are not retained under chromatographic reverse phase conditions (Figure S3A-B), a vacuum liquid chromatography (VLC) system was employed with a Zeoprep 60 C18 15-25 μm reverse phase (Zeochem[®] Silicagel, Rütli, Switzerland). After equilibration with 1L of water, 2 to 2.5 g of extract previously suspended in water and sonicated for 15 minutes were deposited on the stationary phase and eluted first with 1L of water and second with 1L of methanol. The fractionation yield was evaluated for the aqueous fraction (F1) at $41\% \pm 1\%$ ($n=3$) and for the methanolic fraction at $50\% \pm 2\%$ ($n=3$), for a total yield of $92 \pm 1\%$ (w/w).

The methanolic fraction obtained by VLC was then fractionated at a large scale on medium pressure liquid chromatography (MPLC). Gradient optimization was performed at high pressure liquid chromatography (HPLC) scale before being transferred to the MPLC system. At HPLC scale, the enriched extract was separated thanks to an Agilent 1260 HPLC system (Agilent Technologies, Santa Clara, CA, USA) equipped with PDA detection on a Zeoprep column (A90 C18, 250 x 4.6 mm i.d., 15-25 mm, Zeochem, Rütli, Switzerland) at a flow of 1 mL/min of water (A) and methanol (B) both with 0.1 % of formic acid (Fisher Scientific, Bishop, UK). After an equilibration time of 20 min, the gradient was optimized from 5 to 25% of B in 10 min, followed by an isocratic step at 25% of B from 10 to 50 min, and finally from 25 to 95% of B from 50 to 70 minutes. Gradient transfer calculation (Challal et al., 2015; Guillaume et al., 2007) indicated the following MPLC conditions: 140 min from 5 to 25% of B, isocratic step at 25% of 515 min, followed by an increase to 95% of B in 258 min for a total of 15h of separation at a flow of 15 mL/min. The MPLC system (Büchi) was equipped with a modules pump C-660, a UV detector C-640, and a fraction collector C-684 and was controlled by the software Sepacore Control. The MPLC column (460 x 49 mm i.d., Büchi) was packed with the same solid phase as the HPLC scale. The methanolic fraction of PN (10 g) was introduced in MPLC by a dry load cell (Challal et al., 2015) and fractionated into 58 fractions of 250 mL, labelled with M for MPLC. All fractions were dried by rotavapor and eventually freeze-dried. After fraction conditioning, the recovery yield of the total MPLC was 83% (w/w). It should be noted that 1.1 g of MG (**2**) precipitated in four fractions (M17 to M20).

A second batch of MPLC was performed on 7 g of the methanolic fraction. Given the observations made on the first MPLC, the isocratic step at 25% of B was maintained for two additional hours. This increase avoided the semi-preparative step required on the first batch of the crucial fractions (M46 to M48) between the end of MG elution and the beginning of the elution of the most apolar compounds as described below. In addition to MG, iriflophenone 3-C- β -glucoside (**1**) and iriflophenone-2-O- α -rhamnoside (**3**) were identified in the second batch of MPLC in fractions M12 and M18, respectively.

For the first MPLC fractionation, all fractions were checked in short chromatographic conditions as described in (Brillatz et al., 2018) on two complementary systems. The first one was an UPLC system (Waters, Milford, MA, USA), equipped with a PDA detector (Waters) and an ELSD set at 45°C, gain 8 (Sedex 85, Sedere, Alfortville, France). The second system was a UHPLC-HRMS-TOF, set as described in (Brillatz et al., 2018). As the goal was the preparation of fractions depleted in MG in sufficient quantities for *in vivo* testing, the fraction control focused on the presence or absence of this constituent. In this first batch, fractions M1 to M14 presented no ELSD signal of MG, whereas fractions M15 to M45 presented MG as the major signal. Notably, precipitation of MG occurred in the fractions

M17 to M20, and the precipitate was separated from its solution, yielding 1.097 g of precipitated MG. In addition to MG, the fractions M15 to M18 contained the second most abundant constituent of NP, identified as iriflophenone 2-O- β -glucoside (**1**). Among the last fractions, M46 to M48 contained other compounds in addition to MG, whereas M49 to M56 were depleted in MG. A step of purification on these three fractions was subsequently implemented, as described below.

For the second MPLC and the semi-preparative fractionations of fraction F4, fractions were monitored by a UHPLC system equipped with PDA, single quadrupole (QMS), and ELSD (UHPLC-PDA-QMS-ELSD). This three-detector system, controlled by MassLynx[®] V4.2 (Waters), was equipped with an Acquity UPLC system (Waters), which included a binary pumping system, an auto-sampler (set at 10°C), a column manager with a pre-column heater (set at 40°C), a PDA detector and an isocratic solvent manager which directed 10% of the flow to the single quadrupole (Acquity QDA, Waters) while adding a flow of 200 mL/min of water-acetonitrile (1:1) containing 0.1% formic acid. The remaining 90% of the flow was directed to an evaporative light scattering detector (ELSD) (Büchi ELS Detector C-650), set at 45°C, gain 8. The QDA, equipped with an ESI source, was set as follows in negative mode: probe temperature 600°C, ESI capillary voltage 1.2 kV, cone voltage 15V, source temperature 120°C, acquisition range 30 to 1250 Da. Fractions were injected (2 μ L) into an Acquity UPLC BEH C18 column (1.7 μ m, 1 x 50 mm) (Waters) and eluted (0.3 mL/min, column temperature set at 40°C) with water (A) and acetonitrile (B), both containing 0.1% formic acid with the following gradient: from 2 to 50% of B from 0 to 3.9 min, 50 to 98% of B from 3.9 to 4.4 min, an isocratic step at 98 % for 1 minute and a re-equilibration step of 2 min.

MG depletion in hinge fractions of the first MPLC

To remove residual amounts of MG in the fractions at the end of MG elution (M46 to M48), an additional purification step was implemented. Gradient optimization was performed on the HPLC system previously described on a Uptisphere strategy column (C18-HQ, 250 x 4.6 mm i.d., 15 μ m, Interchim, Montluçon, France) before its transfer to Flash chromatography performed on an Interchim system equipped with UV detection. The gradient was optimized as followed: isocratic step at 35% of B for 20 min, followed by a gradient from 35 to 100 % of B in 30 min. Gradient transfer calculation (Challal et al., 2015) indicated the following conditions for a Puriflash column (PF-C18HP, 224 x 36 mm i.d., Interchim, Montluçon, France): isocratic step at 35 % of B for 55 min, followed by a gradient to 100% of B in 82 min at a flow of 12 mL/min. A dry load injection was used to purify 400 mg of a mixture of the three fractions proportional to their MPLC yield, mixed with 2 g of Zeoprep 60 stationary phase (C18 40-63 μ m, Zeochem, Rütli, Switzerland). Three fractions were generated, two of which were depleted in MG and represented 46 % of the loaded quantity. This additional purification was performed on the first batch of MPLC fractions only and was not required for the second MPLC batch due to the increased time of the isocratic steps.

Purification of fraction F4 constituents

Given the *in vivo* results, the F4 fraction was fractionated to formally identify its constituents. Gradient optimization was performed on the same HPLC system described above on a X-bridge C18 column (250 x 4.6 mm i.d., 5 μ m, Waters, Milford, MA, USA) equipped with a pre-column cartridge holder (20 x

4.6 mm i.d., 5 μ m, Waters, Milford, MA, USA). After an equilibration time of 20 min, the optimized gradient was from 22 to 40% of B in 100 min, and from 40 to 100% in 30 min.

Semi-preparative HPLC-UV separation was conducted on a Shimadzu system controlled by the LabSolutions software (Shimadzu, Kyoto, Japan) equipped with a LC-20A module pumps, an SPD-20A UV/VIS, a 77251 Rheodyne[®] valve and an FRC-10A fraction collector (Shimadzu). The column was a X-bridge C18 (250 x 19 mm i.d., 5 μ m, Waters, Milford, MA, USA) equipped with a Waters C18 pre-column cartridge holder (10 x 19 mm i.d.). Gradient transfer calculation (Challal et al., 2015) indicated the following conditions: from 22 to 40 % of B in 103 min and to 100% in 32 min, at a flow of 17 mL/min. Two injections were performed by dry loading, by mixing F4 with stationary phase (Zeoprep[®] C18 40-63 μ m, Rütli, Switzerland), respectively 50 mg of F4 with 70 mg of stationary phase and 25 mg of F4 with 230 mg, according to the protocol developed in (Queiroz et al., 2019). This step permitted to isolate and identify: 2'-O-acetylmangiferin (**4**) (1.6 mg), 2-C- β -glucofuranosylmangiferin (**5**) (0.2 mg), isovitexin (**6**) (0.5 mg), 2-C- α -glucofuranosylmangiferin (0.1 mg) (**7**), 6'-O-acetylmangiferin (**8**) (2.7 mg), genkwanin-5-O- β -primeveroside (**9**) (2.1 mg) and genkwanin-O- β -glucoside (**10**) (0.1 mg) (see Figure 5A for the structure of **6**, **9** and **10**, and Figure S5B for the structure of **4**, **5**, **7** and **8**).

Fraction preparation and dosage for *in vivo* testing

The MPLC MG-free fractions were grouped according to their weight proportion: fractions M1 to M14 were grouped to prepare the fraction labelled F2, fractions M15 to M18 constituted the fraction F3 and fractions M46 to M56 constituted the fraction F4 after further depletion in MG of M46 to M48 as described above. Then, mice dosages were estimated by including the fractionation yield of grouped fractions, corrected by the yield of MPLC (83%) and VLC (50%) which were considered to define a proportional dosage, considering each step of the fractionation process. Thus, fraction F2 represented 13.7% of PN extract, fraction F3, 9.8% and F4, 10.3%, and mice doses were adapted proportionally. Eventually, to verify the fractionation process, the four fractions (F1 to F4) were proportionally pooled and analyzed by UHPLC-CAD, which demonstrated the similarity between the decoction and the reconstituted extract (Figure S4F).

To test *in vivo* the compounds identified in the F4 fraction (GE, AP) and their potential metabolites biotransformed in the digestive system after ingestion, standard substances of IX, GG, GE and AP were purchased. Only GP could not be obtained, and the assay was performed with the fraction M50 of the first MPLC, which contained mainly this constituent. To estimate the proportion of these compounds, chemical profiling obtained by UHPLC-PDA-QDA-MS-ELSD was employed. ELSD peak areas were used to estimate the proportions of IX (4%) and AP (4%), GP (20%), GG (4%) and GE (4%). Mice doses were adjusted proportionally.

Characterization of isolated constituents

All isolated constituents (**1-10**) were analyzed to determine their chemical structure. NMR spectra were recorded on a Bruker Avance III HD 600 MHz NMR spectrometer equipped with a CQI 5 mm Cryoprobe and a SampleJet automated sample changer (Bruker BioSpin). Chemical shift were reported in parts per million (δ) using the deuterated dimethyl sulfoxide (DMSO-*d*₆) signal (δ _H 2.50; δ _C 39.5) as internal

standards for ^1H and ^{13}C NMR, respectively, and coupling constants (J) were reported in hertz. Assignments were obtained based on two-dimensional (2D) NMR experiments (COSY, NOESY, HSQC and HMBC). Accurate masses were measured with the UHPLC-HRMS/MS system described above in the following conditions: samples were injected (1 μL) into an Acquity UPLC BEH C18 column (2.1 x 100 mm i.d. 1.7 μm , Waters, Milford, MA, USA) and eluted (0.6 mL/min, column temperature set at 40°C) with water (A) and acetonitrile (B) both containing 0.1% formic acid with the following gradient: from 5 to 100% of B from 0 to 7 min (curve 6), an isocratic step at 100 % for 1 minutes and a re-equilibration step of 1.9 min. The full MS analyses were performed in negative mode with a mass range of 150-1800 at a resolution of 35000 full width at half maximum (FWHM) (at m/z 200). The optimized HESI-II parameters were the following: source voltage: 2.5 kV (neg); sheath gas flow rate (N_2): 55 units, auxiliary gas flow rate: 15 units, spare gas flow rate: 3; capillary temperature: 450°C; S-Lens RF Level: 45.

Optical rotations were measured for the constituents **4**, **5** and **7**, and were obtained in a 10 cm cell on a Jasco polarimeter (Easton, USA). UV spectra of **4**, **5** and **7** were acquired on a Hach UV-vis DR/4000 instrument (Loveland, CO, USA).

Description of the isolated compounds

The structures are provided in Figure 5 for compounds **6**, **9** and **10**, and in Figure S5B for compounds **4**, **5**, **7** and **8**.

The identification of the following known compounds was supported by NMR spectral data comparison with those of literature: iriflophenone 3-C- β -glucoside (**1**) (Severi et al., 2009), mangiferin (**2**) (Severi et al., 2009), iriflophenone 2-O- α -rhamnoside (**3**) (Hara et al., 2008), isovitexin (**6**) (Pedras et al., 2003), 6'-O-acetylmangiferin (**8**) (Markham and Wallace, 1980), genkwanin 5-O- β -primeveroside (**9**) (Kitalong, C. et al., 2012), and genkwanin-5-O- β -glucoside (**10**) (Veit et al., 1990).

An additional acetylmangiferin, 2'-O-acetylmangiferin (**4**) was identified, which was never reported to our knowledge. The position of the acetate was defined thanks to correlations from the carbonyl at δ_{C} 168.5 to the methyl at δ_{H} 1.73 and to the methine H-2' of the glucose at δ_{H} 5.45 observed on the 2D HMBC spectrum. Furthermore, two additional isomers of MG were described for the first time to our knowledge. They were identified as 2-C- β -glucofuranosylmangiferin (**5**) and 2-C- α -glucofuranosylmangiferin (**7**). The presence of glucofuranosyl moieties in **5** and **7** instead of a glucopyranosyl as in MG (**2**) were proved by the low field ^{13}C NMR chemical shift of C-4' (δ_{C} 79.9 and 80.3 for β and α , respectively) and the high field ^{13}C NMR chemical shift of C-5' (δ_{C} 68.4 for β and α) indicating a free hydroxyl group in C-5' and an ether in C-4'. The ROESY correlation between H-1' and H-4' in compound **5** indicated the α configuration of H-1' whereas no correlation was observed between these two protons in **7**.

Iriflophenone 3-C- β -glucoside (1). Amorphous solid; ^1H NMR (DMSO- d_6 , 600 MHz) δ 3.20 (3H, m, H-3', H-4', H-5'), 3.49 (1H, dd, $J=11.3, 4.3$ Hz, H-6'b), 3.58 (1H, t, $J=9.5$ Hz, H-2'), 3.62 (1H, d, $J=11.3$ Hz, H-6'a), 4.59 (1H, d, $J=9.5$ Hz, H-1'), 5.95 (1H, s, H-5), 6.78 (2H, d, $J=8.7$ Hz, H-10, H-12), 7.56 (2H, d, $J=8.7$ Hz, H-9, H-13); ^{13}C NMR (DMSO- d_6 , 151 MHz) δ 60.5 (C-6'), 69.7 (C-4'), 71.9 (C-2'),

74.7 (C-1'), 78.3 (C-3'), 81.1 (C-5'), 94.8 (C-5), 103.7 (C-3), 107.0 (C-1), 114.6 (C-10, C-12), 130.8 (C-8), 131.5 (C-9, C-13), 156.7 (C-6), 157.4 (C-2), 159.0 (C-4), 161.4 (C-11), 194.6 (C-7). HRESIMS m/z 407.0979 [M-H]⁻ (calculated for C₁₉H₁₉O₁₀, 407.0978, Δppm 0.3). Observed UV max in UHPLC-PDA: 294 nm. SMILES:

C1=CC(O)=C(C(C2=CC=C(O)C=C2)=O)C(O)=C1[C@H]3[C@H](O)[C@@H](O)[C@H](O)[C@@H](CO)C3. InChIKey: BQRGILCJOGVSOP-ACTWTFVSA-N (Severi et al., 2009).

Mangiferin (2) (MG). Clear yellow crystalline solid; ¹H NMR (DMSO-*d*₆, 600 MHz) δ 3.12 (1H, m, H-4'), 3.16 (1H, m, H-5'), 3.19 (1H, m, H-3'), 3.39 (1H, dd, *J*=12.4, 5.1 Hz, H-6'b), 3.68 (2H, d, *J*=12.4 Hz, H-6'a), 4.04 (1H, t, *J*=9.8 Hz, H-2'), 4.47 (1H, t, *J*=6.2, 5.3 Hz, 6'OH), 4.59 (1H, d, *J*=9.8 Hz, H-1'), 6.36 (1H, s, H-4), 6.86 (1H, s, H-5), 7.38 (1H, s, H-8), 13.75 (1H, s, 1OH); ¹³C NMR (DMSO-*d*₆, 151 MHz) δ 61.5 (C-6'), 70.2 (C-2'), 70.6 (C-4'), 73.1 (C-1'), 79.0 (C-3'), 81.6 (C-5'), 93.3 (C-4), 101.3 (C-9a), 102.6 (C-5), 107.6 (C-2), 108.1 (C-8), 111.7 (C-8a), 143.7 (C-7), 150.8 (C-10a), 154.0 (C-6), 156.2 (C-4a), 161.8 (C-1), 163.8 (C-3), 168.9, 179.1 (C-9). HRESIMS m/z 421.0776 [M-H]⁻ (calculated for C₁₉H₁₇O₁₁, 421.0771, Δppm 1.2). Observed UV max in UHPLC-PDA: 258, 318, 365 nm. SMILES: O=C1C2=C(C=C(O)C([C@H]3[C@H](O)[C@@H](O)[C@H](O)[C@@H](CO)O3)=C2O)OC4=CC(O)=C(O)C=C41. InChIKey: AEDDIBAIWPIIBD-ZJKJAXBQSA-N (Severi et al., 2009).

Iriflophenone 2-O-α-rhamnoside (3). Amorphous solid; ¹H NMR (DMSO-*d*₆, 600 MHz) δ 1.04 (3H, d, *J*=6.2 Hz, H-6'), 3.07 (1H, d, *J*=9.5 Hz, H-3'), 3.13 (1H, t, *J*=9.5 Hz, H-4'), 3.27 (1H, m, H-5'), 3.32 (1H, m, H-2'), 5.10 (1H, d, *J*=1.7 Hz, H-1'), 6.03 (1H, d, *J*=2.0 Hz, H-5), 6.13 (1H, d, *J*=2.0 Hz, H-3), 6.79 (2H, d, *J*=8.5 Hz, H-10, H-12), 7.54 (2H, d, *J*=8.5 Hz, H-9, H-13); ¹³C NMR (DMSO-*d*₆, 151 MHz) δ 17.7 (C-6'), 69.3 (C-5'), 69.8 (C-2', C-3'), 71.3 (C-4'), 98.7 (C-1'), 109.3 (C-1), 114.8 (C-10, C-12), 131.2 (C-9, C-13), 155.4 (C-2), 156.2 (C-6), 159.2 (C-4), 161.5 (C-11), 192.5 (C-7). HRESIMS m/z 391.1033 [M-H]⁻ (calculated for C₁₉H₁₉O₉, 391.1029, Δppm 0.9). Observed UV max in UHPLC-PDA: 291 nm. Smiles: OC1=CC(O)=C(C(C2=CC=C(O)C=C2)=O)C(O[C@@H]3O[C@@H](C)[C@H](O)[C@@H](O)[C@H]3O)=C1. InChIKey: BDUFDLBIUJUAJE-KONKAKAUSA-N (Hara et al., 2008).

2'-O-Acetylmangiferin (4). Amorphous solid; [α]²⁰_D +81 (±4 (SD, n=5)), c 0.075, MeOH), UV □_{max} (MeOH) (log □) 241 (4.27), 256 (4.22), 314 (3.91) 367 (3.92) nm; ¹H NMR (DMSO-*d*₆, 600 MHz, T=343K) δ 1.73 (3H, s, H-2'b), 3.28 (1H, m, H-5'), 3.31 (1H, t, *J*=9.0 Hz, H-4'), 3.46 (1H, d, *J*=8.7 Hz, H-3'), 3.51 (1H, m, H-6'b), 3.73 (1H, m, H-6'a), 4.83 (1H, d, *J*=10.0 Hz, H-1'), 5.45 (1H, t, *J*=9.6 Hz, H-2'), 6.33 (1H, s, H-4), 6.83 (1H, s, H-5), 7.39 (1H, s, H-8), 13.73 (1H, s, 1OH); ¹³C NMR (DMSO-*d*₆, 151 MHz, T=343K) δ 20.2 (C-2'b), 61.0 (C-6'), 70.3 (C-4'), 70.5 (C-1'), 72.2 (C-2'), 75.9 (C-3'), 81.2 (C-5'), 93.1 (C-4), 100.8 (C-9a), 102.3 (C-5), 105.4 (C-2), 107.8 (C-8), 111.4 (C-8a), 143.6 (C-7), 150.7 (C-10a), 154.1 (C-6), 156.2 (C-4a), 161.3 (C-1), 163.5 (C-3), 168.5 (C-2'a), 178.7 (C-9). HRESIMS m/z 463.0902 [M-H]⁻ (calculated for C₂₁H₁₉O₁₂, 463.0877, Δppm 5.4). SMILES: O=C1C2=C(C=C(O)C([C@@H]3O[C@H](CO)[C@@H](O)[C@H](O)[C@H]3OC(C)=O)=C2O)OC4=C(O)C(O)C=C41. InChIKey: ZWQDCGBIYCPHCX-DPEQZQOSSA-N.

2-C-β-Glucofuranosylmangiferin (5). Amorphous solid; [α]²⁰_D +146 (±16 (SD, n=5)), c 0.010, MeOH), UV λ_{max} (MeOH) (log ε) 241 (4.24), 257 (4.26), 316 (3.98) 365 (3.85) nm; ¹H NMR (DMSO-*d*₆, 600 MHz)

δ 3.39 (OH, dd, $J=11.3, 5.9$ Hz, H-6'b), 3.56 (1H, dd, $J=11.3, 3.0$ Hz, H-6'a), 3.70 (1H, dd, $J=8.6, 2.6$ Hz, H-4'), 3.77 (1H, ddd, $J=8.76, 5.9, 3.0$ Hz, H-5'), 4.03 (1H, d, $J=2.6$ Hz, H-3'), 4.06 (1H, t, $J=3.5$ Hz, H-2'), 5.07 (1H, d, $J=3.5$ Hz, H-1'), 6.29 (1H, d, $J=7.1$ Hz, H-4), 6.84 (1H, s, H-5), 7.37 (1H, s, H-8), 13.95 (1H, s, 1OH); ^{13}C NMR (DMSO- d_6 , 151 MHz) δ 63.6 (C-6'), 68.4 (C-5'), 76.8 (C-3'), 79.3 (C-1'), 79.9 (C-4'), 81.1 (C-2'), 94.2 (C-4), 100.5 (C-9a), 102.4 (C-5), 106.8 (C-2), 107.7 (C-8), 111.3 (C-8a), 143.5 (C-7), 150.6 (C-6), 153.9 (C-10a), 160.1 (C-1), 163.2 (C-3), 178.6 (C-9). HRESIMS m/z 421.0791 [M-H]⁻ (calculated for C₁₉H₁₇O₁₁, 421.0771, Δ ppm 4.8). SMILES: O=C1C2=C(C=C(O)C([C@H]3[C@H](O)[C@@H](O)[C@H](O3)[C@H](CO)O)=C2O)OC4=CC(O)=C(O)C=C41. InChIKey: ULVKMRNLBMAPTI-BBNFYSXSA-N.

Isovitexin (6) (IX). Amorphous solid; ^1H NMR (DMSO- d_6 , 600 MHz) δ 3.12 (1H, t, $J=9.0$ Hz, H-4"), 3.16 (1H, m, H-5"), 3.20 (1H, t, $J=8.7$ Hz, H-3"), 3.41 (1H, m, H-6"b), 3.68 (1H, m, H-6"a), 4.03 (1H, t, $J=8.9$ Hz, H-2"), 4.58 (1H, d, $J=9.7$ Hz, H-1"), 6.51 (1H, s, H-8), 6.79 (1H, s, H-3), 6.93 (2H, d, $J=8.8$ Hz, H-3', H-5'), 7.93 (2H, d, $J=8.8$ Hz, H-2', H-6'), 13.55 (1H, s, 5OH); ^{13}C NMR (DMSO- d_6 , 151 MHz) δ 61.5 (C-6"), 70.2 (C-2"), 70.6 (C-4"), 73.0 (C-1"), 78.9 (C-3"), 81.6 (C-5"), 103.4 (C-10), 108.9 (C-6), 116.0 (C-3', C-5'), 128.5 (C-2', C-6'), 156.2 (C-9), 160.7 (C-5), 161.2 (C-4'), 163.4 (C-7), 163.5 (C-2), 182.0 (C-4). HRESIMS m/z 431.0999 [M-H]⁻ (calculated for C₂₁H₁₉O₁₀, 431.0978, Δ ppm 4.8). Observed UV max in UHPLC-PDA: 259, 323 nm. SMILES: O=C1C=C(C2=CC=C(O)C=C2)OC3=CC(O)=C([C@H]4O[C@@H](CO)[C@H](O)[C@@H](O)[C@@H]4O)C(O)=C31. InChIKey: MYXNWGACZJSMBT-UBFQGWSSASA-N (Pedras et al., 2003).

2-C- α -Glucofuranosylmangiferin (7). Amorphous solid; $[\alpha]_D^{20} + 232$ (± 12 (SD, $n=5$), c 0.005, MeOH), UV λ_{max} (MeOH) (log ϵ) 241 (4.50), 257 (4.50), 316 (4.26) 365 (4.10) nm; ^1H NMR (DMSO- d_6 , 600 MHz) δ 3.48 (1H, dd, $J=10.9, 5.2$ Hz, H-6'b), 3.59 (1H, m, H-6'a), 3.78 (1H, m, H-5'), 4.16 (2H, m, H-3', H-4'), 4.20 (1H, t, $J=1.8, 1.4$ Hz, H-2'), 4.52 (1H, t, $J=5.7$ Hz, 6'OH), 4.65 (1H, d, $J=6.0$ Hz, 5'OH), 5.33 (1H, d, $J=3.7$ Hz, 3'OH), 5.51 (1H, d, $J=2.9$ Hz, H-1'), 6.30 (1H, s, H-4), 6.86 (1H, s, H-5), 7.38 (1H, s, H-8), 13.72 (1H, s, 1OH); ^{13}C NMR (DMSO- d_6 , 151 MHz) δ 63.8 (C-6'), 68.4 (C-5'), 74.9 (C-3'), 77.1 (C-2'), 79.3 (C-1'), 80.3 (C-4'), 94.2 (C-4), 101.0 (C-9a), 102.6 (C-5), 108.0 (C-8), 111.7 (C-8a), 143.8 (C-7), 150.9 (C-10a), 154.1 (C-6), 156.1 (C-4a), 159.2 (C-1), 164.5 (C-3), 179.0 (C-9). HRESIMS m/z 421.0792 [M-H]⁻ (calculated for C₁₉H₁₇O₁₁, 421.0771, Δ ppm 4.9). SMILES: O=C1C2=C(C=C(O)C([C@@H]3[C@H](O)[C@@H](O)[C@H](O3)[C@H](CO)O)=C2O)OC4=CC(O)=C(O)C=C41. InChIKey: ULVKMRNLBMAPTI-QRDWVMTRSA-N.

6'-O-Acetylmangiferin (8). Amorphous solid; ^1H NMR (DMSO- d_6 , 600 MHz) δ 1.98 (3H, s, H-6'b), 3.16 (1H, t, $J=8.7$ Hz, H-4'), 3.21 (1H, t, $J=8.7$ Hz, H-3'), 3.37 (1H, m, H-5'), 3.90 (1H, dd, $J=12.0, 7.0$ Hz, H-6'b), 4.09 (1H, t, $J=9.9, 8.7$ Hz, H-2'), 4.35 (1H, dd, $J=12.0, 1.8$ Hz, H-6'a), 4.59 (1H, d, $J=9.8$ Hz, H-1'), 6.37 (1H, s, H-4), 6.86 (1H, s, H-5), 7.37 (1H, s, H-8), 13.78 (1H, s, 1OH); ^{13}C NMR (DMSO- d_6 , 151 MHz) δ 20.8 (C-6'b), 64.6 (C-6'), 69.9 (C-2'), 70.4 (C-4'), 73.1 (C-1'), 78.1 (C-5'), 78.7 (C-3'), 93.2 (C-4), 101.3 (C-9a), 102.6 (C-5), 107.3 (C-2), 108.0 (C-8), 111.6 (C-8a), 143.8 (C-7), 150.8 (C-10a), 154.1 (C-6), 156.2 (C-4a), 161.9 (C-1), 163.8 (C-3), 170.4 (C-6'a), 179.1 (C-9). HRESIMS m/z 463.0900 [M-H]⁻ (calculated for C₂₁H₁₉O₁₂, 463.0877, Δ ppm 5.0). Observed UV max in UHPLC-PDA: 257, 317, 366 nm. SMILES:

O=C1C2=C(C=C(O)C([C@@H]3O[C@H](COC(C)=O)[C@@H](O)[C@H](O)[C@H]3O)=C2O)OC4=C(C(O)=C(O)C=C41. InChIKey: MJZHKT MNVNMAPP-RDZBXBSQSA-N (Markham and Wallace, 1980).

Genkwanin 5-O- β -primeveroside (9) (GP) (synonym *yuankanin*): Amorphous solid; ¹H NMR (DMSO-d₆, 600 MHz) δ 2.98 (1H, td, J=8.3, 4.8 Hz, H-2''), 3.03 (1H, t, J=10.8 Hz, H-5''b), 3.10 (1H, td, J=8.8, 4.6 Hz, H-3''), 3.21 (1H, td, J=9.1, 5.3 Hz, H-4''), 3.28 (1H, m, H-4''), 3.29 (1H, m, H-3''), 3.36 (1H, m, H-2''), 3.57 (1H, ddd, J=8.8, 6.5, 1.9 Hz, H-5''), 3.65 (1H, dd, J=11.4, 6.6 Hz, H-6''b), 3.69 (1H, dd, J=11.3, 5.4 Hz, H-5''a), 3.90 (3H, s, 7OMe), 3.98 (1H, dd, J=11.5, 1.9 Hz, H-6''a), 4.19 (1H, d, J=7.6 Hz, H-1''), 4.78 (1H, d, J=7.6 Hz, H-1''), 4.87 (1H, d, J=5.0 Hz, 2''OH), 4.94 (2H, d, J=4.8 Hz, 3''OH, 4''OH), 5.17 (1H, d, J=5.6 Hz, 4''OH), 5.18 (1H, d, J=6.0 Hz, 3''OH), 5.59 (1H, d, J=2.0 Hz, 2''OH), 6.72 (1H, s, H-3), 6.88 (1H, d, J=2.4 Hz, H-6), 6.92 (2H, d, J=8.7 Hz, H-3', H-5'), 7.04 (1H, d, J=2.4 Hz, H-8), 7.93 (2H, d, J=8.8 Hz, H-2', H-6'), 10.28 (1H, s, 4'OH); ¹³C NMR (DMSO-d₆, 151 MHz) δ 56.1 (C-7OMe), 65.7 (C-5''), 68.7 (C-6''), 69.5 (C-4''), 69.8 (C-4''), 73.4 (C-2''), 73.5 (C-2''), 75.6 (C-3''), 75.9 (C-5''), 76.6 (C-3''), 96.7 (C-8), 103.0 (C-6), 103.8 (C-1''), 104.1 (C-1''), 105.8 (C-3), 109.2 (C-10), 115.9 (C-3', C-5'), 121.1 (C-1'), 128.2 (C-2', C-6'), 158.1 (C-5), 158.4 (C-9), 160.9 (C-4'), 161.3 (C-2), 163.6 (C-7), 176.9 (C-4). HRESIMS *m/z* 577.1585 [M-H]⁻ (calculated for C₂₇H₂₉O₁₄, 577.1557, Δ ppm 4.8). Observed UV max in UHPLC-PDA: 260, 330 nm SMILES: O[C@H]([C@H]([C@@H]([C@H](O1)CO[C@H]2[C@H](O)[C@@H](O)[C@H](O)CO2)O)O)[C@@H]1OC3=CC(OC)=CC(OC(C4=CC=C(C=C4)O)=C5)=C3C5=O. InChIKey: ZKIXACXWZQFVAB-MUCJXJSVSA-N (Hara et al., 2008).

Genkwanin 5-O- β -glucoside (10) (GG), (synonym *glucogenkwanin*): Amorphous solid; ¹H NMR (DMSO-d₆, 600 MHz) δ 3.15 (1H, m, H-4''), 3.28 (1H, m, H-3''), 3.35 (1H, m, H-2''), 3.36 (1H, m, H-5''), 3.50 (1H, dt, J=12.1, 6.1 Hz, H-6''b), 3.90 (3H, s, 7OMe), 4.71 (1H, t, J=6.0 Hz, 6''OH), 4.75 (1H, d, J=7.7 Hz, H-1''), 5.07 (1H, d, J=5.4 Hz, 4''OH), 5.12 (1H, d, J=5.2 Hz, 3''OH), 5.61 (1H, d, J=1.8 Hz, 2''OH), 6.73 (1H, s, H-3), 6.91 (1H, d, J=2.4 Hz, H-6), 6.92 (2H, d, J=8.8 Hz, H-3', H-5'), 7.07 (1H, d, J=2.4 Hz, H-8), 7.94 (2H, d, J=8.8 Hz, H-2', H-6'), 10.29 (1H, s, 4'OH); ¹³C NMR (DMSO-d₆, 151 MHz) δ 55.8 (C-7OMe), 60.7 (C-6''), 69.7 (C-4''), 73.4 (C-2''), 75.5 (C-3''), 77.4 (C-5''), 96.4 (C-8), 103.3 (C-6), 104.0 (C-1''), 105.5 (C-3), 108.9 (C-10), 115.7 (C-3'), 120.8 (C-1'), 128.0 (C-2'), 157.9 (C-5), 158.1 (C-9), 160.5 (C-4'), 161.1 (C-2), 163.2 (C-7). HRESIMS *m/z* 445.1155 [M-H]⁻ (calculated for C₂₂H₂₁O₁₀, 445.1135, Δ ppm 4.5). Observed UV max in UHPLC-PDA: 262, 327 nm. SMILES: COC1=CC(O[C@H]2[C@@H]([C@H]([C@@H]([C@H](O2)CO)O)O)O)=C3C(C=C(OC3=C1)C(C=C4)=CC=C4O)=O. InChIKey: QLZMOQILAYMPIF-MIUGBVLSSA-N (Veit et al., 1990).

References

- Abel, E.D., Peroni, O., Kim, J.K., Kim, Y.B., Boss, O., Hadro, E., Minnemann, T., Shulman, G.I., and Kahn, B.B. (2001). Adipose-selective targeting of the GLUT4 gene impairs insulin action in muscle and liver. *Nature* *409*, 729–733.
- Apontes, P., Liu, Z., Su, K., Benard, O., Youn, D.Y., Li, X., Li, W., Mirza, R.H., Bastie, C.C., Jelicks, L.A., et al. (2014). Mangiferin stimulates carbohydrate oxidation and protects against metabolic disorders induced by high-fat diets. *Diabetes* *63*, 3626–3636.
- Bailey, C.J. (2017). Metformin: historical overview. *Diabetologia* *60*, 1566–1576.
- Balaz, M., Becker, A.S., Balazova, L., Straub, L., Müller, J., Gashi, G., Maushart, C.I., Sun, W., Dong, H., Moser, C., et al. (2019). Inhibition of mevalonate pathway prevents adipocyte browning in mice and men by affecting protein prenylation. *Cell Metab* *29*, 901-916.e8.
- Beaton, N., Rudigier, C., Moest, H., Müller, S., Mrosek, N., Röder, E., Rudofsky, G., Rüllicke, T., Ukropec, J., Ukropcova, B., et al. (2015). TUSC5 regulates insulin-mediated adipose tissue glucose uptake by modulation of GLUT4 recycling. *Mol Metab* *4*, 795–810.
- de Boer, Y.S., and Sherker, A.H. (2017). Herbal and dietary supplement-induced liver injury. *Clin Liver Dis* *21*, 135–149.
- Bosch, R.R., Bazuine, M., Span, P.N., Willems, P.H.G.M., Olthaar, A.J., van Rennes, H., Maassen, J.A., Tack, C.J., Hermus, A.R.M.M., and Sweep, C.G.J.F. (2004). Regulation of GLUT1-mediated glucose uptake by PKC λ -PKC β (II) interactions in 3T3-L1 adipocytes. *Biochem J* *384*, 349–355.
- Brillatz, T., Lauritano, C., Jacmin, M., Khamma, S., Marcourt, L., Righi, D., Romano, G., Esposito, F., Ianora, A., Queiroz, E.F., et al. (2018). Zebrafish-based identification of the antiseizure nucleoside inosine from the marine diatom *Skeletonema marinoi*. *PLoS One* *13*, e0196195.
- Buse, M.G., Robinson, K.A., Marshall, B.A., and Mueckler, M. (1996). Differential effects of GLUT1 or GLUT4 overexpression on hexosamine biosynthesis by muscles of transgenic mice. *J Biol Chem* *271*, 23197–23202.
- Chadt, A., and Al-Hasani, H. (2020). Glucose transporters in adipose tissue, liver, and skeletal muscle in metabolic health and disease. *Pflugers Arch* *472*, 1273–1298.
- Challal, S., Queiroz, E.F., Debrus, B., Kloeti, W., Guillarme, D., Gupta, M.P., and Wolfender, J.-L. (2015). Rational and efficient preparative isolation of natural products by MPLC-UV-ELSD based on HPLC to MPLC gradient transfer. *Planta Med* *81*, 1636–1643.
- Chin, S.H., Item, F., Wueest, S., Zhou, Z., Wiedemann, M.S.F., Gai, Z., Schoenle, E.J., Kullak-Ublick, G.A., Al-Hasani, H., and Konrad, D. (2015). Opposing effects of reduced kidney mass on liver and skeletal muscle insulin sensitivity in obese mice. *Diabetes* *64*, 1131–1141.
- Ciaraldi, T.P., Mudaliar, S., Barzin, A., Macievic, J.A., Edelman, S.V., Park, K.S., and Henry, R.R. (2005). Skeletal muscle GLUT1 transporter protein expression and basal leg glucose uptake are reduced in type 2 diabetes. *J Clin Endocrinol Metab* *90*, 352–358.
- Corcoran, C., and Jacobs, T.F. (2021). Metformin. In *StatPearls*, (Treasure Island (FL): StatPearls Publishing)
- Ehrenkranz, J.R.L., Lewis, N.G., Kahn, C.R., and Roth, J. (2005). Phlorizin: a review. *Diabetes Metab Res Rev* *21*, 31–38.
- Elabd, C., Chiellini, C., Carmona, M., Galitzky, J., Cochet, O., Petersen, R., Pénicaud, L., Kristiansen, K., Bouloumié, A., Casteilla, L., et al. (2009). Human multipotent adipose-derived stem cells differentiate into functional brown adipocytes. *Stem Cells* *27*, 2753–2760.

- Foretz, M., Hébrard, S., Leclerc, J., Zarrinpashneh, E., Soty, M., Mithieux, G., Sakamoto, K., Andreelli, F., and Viollet, B. (2010). Metformin inhibits hepatic gluconeogenesis in mice independently of the LKB1/AMPK pathway via a decrease in hepatic energy state. *J Clin Invest* 120, 2355–2369.
- Garvey, W.T., Maianu, L., Huecksteadt, T.P., Birnbaum, M.J., Molina, J.M., and Ciaraldi, T.P. (1991). Pretranslational suppression of a glucose transporter protein causes insulin resistance in adipocytes from patients with non-insulin-dependent diabetes mellitus and obesity. *J Clin Invest* 87, 1072–1081.
- Garvey, W.T., Maianu, L., Zhu, J.H., Brechtel-Hook, G., Wallace, P., and Baron, A.D. (1998). Evidence for defects in the trafficking and translocation of GLUT4 glucose transporters in skeletal muscle as a cause of human insulin resistance. *J Clin Invest* 101, 2377–2386.
- Gaster, M., Staehr, P., Beck-Nielsen, H., Schrøder, H.D., and Handberg, A. (2001). GLUT4 is reduced in slow muscle fibers of type 2 diabetic patients: Is insulin resistance in type 2 diabetes a slow, type 1 fiber disease? *Diabetes* 50, 1324–1329.
- Ge, X., Chen, C., Hui, X., Wang, Y., Lam, K.S.L., and Xu, A. (2011). Fibroblast growth factor 21 induces glucose transporter-1 expression through activation of the serum response factor/Ets-like protein-1 in adipocytes. *J Biol Chem* 286, 34533–34541.
- Grandl, G., Straub, L., Rudigier, C., Arnold, M., Wueest, S., Konrad, D., and Wolfrum, C. (2018). Short-term feeding of a ketogenic diet induces more severe hepatic insulin resistance than an obesogenic high-fat diet. *J Physiol* 596, 4597–4609.
- Graz, B., Kitalong, C., and Yano, V. (2015). Traditional local medicines in the republic of Palau and non-communicable diseases (NCD), signs of effectiveness. *J Ethnopharmacol* 161, 233–237.
- Guillarme, D., Nguyen, D.T.-T., Rudaz, S., and Veuthey, J.-L. (2007). Method transfer for fast liquid chromatography in pharmaceutical analysis: application to short columns packed with small particle. Part I: isocratic separation. *Eur J Pharm Biopharm* 66, 475–482.
- Hara, H., Ise, Y., Morimoto, N., Shimazawa, M., Ichihashi, K., Ohyama, M., and Iinuma, M. (2008). Laxative effect of agarwood leaves and its mechanism. *Biosci Biotechnol Biochem* 72, 335–345.
- Heilig, C., Brosius, F., Siu, B., Concepcion, L., Mortensen, R., Heilig, K., Zhu, M., Weldon, R., Wu, G., and Conner, D. (2003). Implications of glucose transporter protein type 1 (GLUT1)-haploinsufficiency in embryonic stem cells for their survival in response to hypoxic stress. *Am J Pathol* 163, 1873–1885.
- Hundal, R.S., Krssak, M., Dufour, S., Laurent, D., Lebon, V., Chandramouli, V., Inzucchi, S.E., Schumann, W.C., Petersen, K.F., Landau, B.R., et al. (2000). Mechanism by Which Metformin Reduces Glucose Production in Type 2 Diabetes. *Diabetes* 49, 2063–2069.
- Ishino, S., Sugita, T., Kondo, Y., Okai, M., Tsuchimori, K., Watanabe, M., Mori, I., Hosoya, M., Horiguchi, T., and Kamiguchi, H. (2017). Glucose uptake of the muscle and adipose tissues in diabetes and obesity disease models: evaluation of insulin and β -adrenergic receptor agonist effects by ^{18}F -FDG. *Ann Nucl Med* 31, 413–423.
- Jung, S.M., Doxsey, W.G., Le, J., Haley, J.A., Mazuecos, L., Luciano, A.K., Li, H., Jang, C., and Guertin, D.A. (2021). In vivo isotope tracing reveals the versatility of glucose as a brown adipose tissue substrate. *Cell Reports* 36, 109459.
- Kaess, B.M., Pedley, A., Massaro, J.M., Murabito, J., Hoffmann, U., and Fox, C.S. (2012). The ratio of visceral to subcutaneous fat, a metric of body fat distribution, is a unique correlate of cardiometabolic risk. *Diabetologia* 55, 2622–2630.
- Kahn, B.B., Rossetti, L., Lodish, H.F., and Charron, M.J. (1991). Decreased in vivo glucose uptake but normal expression of GLUT1 and GLUT4 in skeletal muscle of diabetic rats. *J Clin Invest* 87, 2197–2206.
- Kahn, S.E., Hull, R.L., and Utzschneider, K.M. (2006). Mechanisms linking obesity to insulin resistance and type 2 diabetes. *Nature* 444, 840–846.

- Kalinovich, A., Dehvari, N., Åslund, A., van Beek, S., Halleskog, C., Olsen, J., Forsberg, E., Zacharewicz, E., Schaart, G., Rinde, M., et al. (2020). Treatment with a β -2-adrenoceptor agonist stimulates glucose uptake in skeletal muscle and improves glucose homeostasis, insulin resistance and hepatic steatosis in mice with diet-induced obesity. *Diabetologia* **63**, 1603–1615.
- Kampmann, U., Christensen, B., Nielsen, T.S., Pedersen, S.B., Ørskov, L., Lund, S., Møller, N., and Jessen, N. (2011). GLUT4 and UBC9 protein expression is reduced in muscle from type 2 diabetic patients with severe insulin resistance. *PLoS One* **6**, e27854.
- Kennedy, J.W., Hirshman, M.F., Gervino, E.V., Ocel, J.V., Forse, R.A., Hoenig, S.J., Aronson, D., Goodyear, L.J., and Horton, E.S. (1999). Acute exercise induces GLUT4 translocation in skeletal muscle of normal human subjects and subjects with type 2 diabetes. *Diabetes* **48**, 1192–1197.
- Khan, A., Unnisa, A., Soheli, M., Date, M., Panpaliya, N., Saboo, S.G., Siddiqui, F., and Khan, S. (2022). Investigation of phytoconstituents of *Enicostemma littorale* as potential glucokinase activators through molecular docking for the treatment of type 2 diabetes mellitus. *In Silico Pharmacol* **10**, 1.
- Khayat, Z.A., Tsakiridis, T., Ueyama, A., Somwar, R., Ebina, Y., and Klip, A. (1998). Rapid stimulation of glucose transport by mitochondrial uncoupling depends in part on cytosolic Ca²⁺ and cPKC. *Am J Physiol* **275**, C1487-1497.
- Kitalong, C., Nogueira, R.C., Benichou, J., Yano, V., Espangel, V., Houriet, J., Rudigier, C., and Graz, B. (2017). “DAK”, a traditional decoction in Palau, as adjuvant for patients with insufficient control of diabetes mellitus type II. *J Ethnopharmacol* **205**, 116–122.
- Kitalong, C., El-Halawany, A. M., El-Dine, R., Ma, C.-m, and Hattori, M. (2012). Phenolics from *Phaleria nissidai* with estrogenic activity. *Rec. Nat. Prod.* 296–300.
- Klein, J., Fasshauer, M., Klein, H.H., Benito, M., and Kahn, C.R. (2002). Novel adipocyte lines from brown fat: a model system for the study of differentiation, energy metabolism, and insulin action. *Bioessays* **24**, 382–388.
- Koivisto, U.M., Martinez-Valdez, H., Bilan, P.J., Burdett, E., Ramlal, T., and Klip, A. (1991). Differential regulation of the GLUT-1 and GLUT-4 glucose transport systems by glucose and insulin in L6 muscle cells in culture. *J Biol Chem* **266**, 2615–2621.
- Kulakowski, D., Kitalong, C., Negrin, A., Tadao, V.-R., Balick, M.J., and Kennelly, E.J. (2015). Traditional preparation of *Phaleria nissidai*, a Palauan tea, reduces exposure to toxic daphnane-type diterpene esters while maintaining immunomodulatory activity. *J Ethnopharmacol* **173**, 273–279.
- Lee, E.E., Ma, J., Sacharidou, A., Mi, W., Salato, V.K., Nguyen, N., Jiang, Y., Pascual, J.M., North, P.E., Shaul, P.W., et al. (2015). A protein kinase C phosphorylation motif in GLUT1 affects glucose transport and is mutated in GLUT1 deficiency syndrome. *Mol Cell* **58**, 845–853.
- Licata, A., Macaluso, F.S., and Craxi, A. (2013). Herbal hepatotoxicity: a hidden epidemic. *Intern Emerg Med* **8**, 13–22.
- Lund, S., Holman, G.D., Schmitz, O., and Pedersen, O. (1995). Contraction stimulates translocation of glucose transporter GLUT4 in skeletal muscle through a mechanism distinct from that of insulin. *Proc Natl Acad Sci U S A* **92**, 5817–5821.
- Madiraju, A.K., Erion, D.M., Rahimi, Y., Zhang, X.-M., Braddock, D.T., Albright, R.A., Prigaro, B.J., Wood, J.L., Bhanot, S., MacDonald, M.J., et al. (2014). Metformin suppresses gluconeogenesis by inhibiting mitochondrial glycerophosphate dehydrogenase. *Nature* **510**, 542–546.
- Madiraju, A.K., Qiu, Y., Perry, R.J., Rahimi, Y., Zhang, X.-M., Zhang, D., Camporez, J.-P.G., Cline, G.W., Butrico, G.M., Kemp, B.E., et al. (2018). Metformin inhibits gluconeogenesis via a redox-dependent mechanism in vivo. *Nat Med* **24**, 1384–1394.
- Markham, K.R., and Wallace, J.W. (1980). C-glycosylxanthone and flavonoid variation within the filmy-ferns (*hymenophyllaceae*). *Phytochemistry* **19**, 415–420.

Matsui, Y., Hirasawa, Y., Sugiura, T., Toyoshi, T., Kyuki, K., and Ito, M. (2010). Metformin reduces body weight gain and improves glucose intolerance in high-fat diet-fed C57BL/6J mice. *Biol Pharm Bull* 33, 963–970.

Montessuit, C., and Thorburn, A. (1999). Transcriptional activation of the glucose transporter GLUT1 in ventricular cardiac myocytes by hypertrophic agonists. *J Biol Chem* 274, 9006–9012.

Nair, A.B., and Jacob, S. (2016). A simple practice guide for dose conversion between animals and human. *J Basic Clin Pharm* 7, 27–31.

NCD Risk Factor Collaboration (NCD-RisC) (2016). Worldwide trends in diabetes since 1980: a pooled analysis of 751 population-based studies with 4.4 million participants. *Lancet* 387, 1513–1530.

Németh, K., Plumb, G.W., Berrin, J.-G., Juge, N., Jacob, R., Naim, H.Y., Williamson, G., Swallow, D.M., and Kroon, P.A. (2003). Deglycosylation by small intestinal epithelial cell beta-glucosidases is a critical step in the absorption and metabolism of dietary flavonoid glycosides in humans. *Eur J Nutr* 42, 29–42.

Nose, A., Mori, Y., Uchiyama-Tanaka, Y., Kishimoto, N., Maruyama, K., Matsubara, H., and Iwasaka, T. (2003). Regulation of glucose transporter (GLUT1) gene expression by angiotensin II in mesangial cells: involvement of HB-EGF and EGF receptor transactivation. *Hypertens Res* 26, 67–73.

Olsen, J.M., Sato, M., Dallner, O.S., Sandström, A.L., Pisani, D.F., Chambard, J.-C., Amri, E.-Z., Hutchinson, D.S., and Bengtsson, T. (2014). Glucose uptake in brown fat cells is dependent on mTOR complex 2-promoted GLUT1 translocation. *J Cell Biol* 207, 365–374.

Owen, M.R., Doran, E., and Halestrap, A.P. (2000). Evidence that metformin exerts its anti-diabetic effects through inhibition of complex 1 of the mitochondrial respiratory chain. *Biochem J* 348 Pt 3, 607–614.

Pedras, M.S.C., Chumala, P.B., and Suchy, M. (2003). Phytoalexins from *Thlaspi arvense*, a wild crucifer resistant to virulent *Leptosphaeria maculans*: structures, syntheses and antifungal activity. *Phytochemistry* 64, 949–956.

Picatoste, B., Yammine, L., Leahey, R.A., Soares, D., Johnson, E.F., Cohen, P., and McGraw, T.E. (2021). Defective insulin-stimulated GLUT4 translocation in brown adipocytes induces systemic glucose homeostasis dysregulation independent of thermogenesis in female mice. *Mol Metab*, 101305.

Preis, S.R., Massaro, J.M., Robins, S.J., Hoffmann, U., Vasan, R.S., Irlbeck, T., Meigs, J.B., Sutherland, P., D'Agostino, R.B., O'Donnell, C.J., et al. (2010). Abdominal subcutaneous and visceral adipose tissue and insulin resistance in the Framingham heart study. *Obesity (Silver Spring)* 18, 2191–2198.

Queiroz, E.F., Alfattani, A., Afzan, A., Marcourt, L., Guillarme, D., and Wolfender, J.-L. (2019). Utility of dry load injection for an efficient natural products isolation at the semi-preparative chromatographic scale. *J Chromatogr A* 1598, 85–91.

Ren, J.M., Semenkovich, C.F., Gulve, E.A., Gao, J., and Holloszy, J.O. (1994). Exercise induces rapid increases in GLUT4 expression, glucose transport capacity, and insulin-stimulated glycogen storage in muscle. *J Biol Chem* 269, 14396–14401.

Schoefer, L., Mohan, R., Schwiertz, A., Braune, A., and Blaut, M. (2003). Anaerobic degradation of flavonoids by *Clostridium orbiscindens*. *Appl Environ Microbiol* 69, 5849–5854.

Severi, J.A., Lima, Z.P., Kushima, H., Brito, A.R.M.S., Santos, L.C. dos, Vilegas, W., and Hiruma-Lima, C.A. (2009). Polyphenols with antiulcerogenic action from aqueous decoction of mango leaves (*Mangifera indica* L.). *Molecules* 14, 1098–1110.

Shen, B. (2015). A New Golden Age of Natural Products Drug Discovery. *Cell* 163, 1297–1300.

van der Stelt, I., Hoevenaars, F., Široká, J., de Ronde, L., Friedecký, D., Keijer, J., and van Schothorst, E. (2017). Metabolic Response of Visceral White Adipose Tissue of Obese Mice Exposed for 5 Days to Human Room Temperature Compared to Mouse Thermoneutrality. *Front Physiol* 8, 179.

- Stolic, M., Russell, A., Hutley, L., Fielding, G., Hay, J., MacDonald, G., Whitehead, J., and Prins, J. (2002). Glucose uptake and insulin action in human adipose tissue--influence of BMI, anatomical depot and body fat distribution. *Int J Obes Relat Metab Disord* 26, 17–23.
- Suman, R.K., Mohanty, I.R., Maheshwari, U., Borde, M.K., and Deshmukh, Y.A. (2016). Natural dipeptidyl peptidase-IV inhibitor mangiferin mitigates diabetes- and metabolic syndrome-induced changes in experimental rats. *Diabetes Metab Syndr Obes* 9, 261–272.
- Taha, C., Tsakiridis, T., McCall, A., and Klip, A. (1997). Glucose transporter expression in L6 muscle cells: regulation through insulin- and stress-activated pathways. *Am J Physiol* 273, E68-76.
- Taylor, E.B., An, D., Kramer, H.F., Yu, H., Fujii, N.L., Roeckl, K.S.C., Bowles, N., Hirshman, M.F., Xie, J., Feener, E.P., et al. (2008). Discovery of TBC1D1 as an insulin-, AICAR-, and contraction-stimulated signaling nexus in mouse skeletal muscle. *J Biol Chem* 283, 9787–9796.
- Todaro, G.J., and Green, H. (1963). Quantitative studies of the growth of mouse embryo cells in culture and their development into established lines. *J Cell Biol* 17, 299–313.
- Tremblay, F., Lavigne, C., Jacques, H., and Marette, A. (2001). Defective insulin-induced GLUT4 translocation in skeletal muscle of high fat-fed rats is associated with alterations in both Akt/protein kinase B and atypical protein kinase C (zeta/lambda) activities. *Diabetes* 50, 1901–1910.
- Tsuru, M., Katagiri, H., Asano, T., Yamada, T., Ohno, S., Ogihara, T., and Oka, Y. (2002). Role of PKC isoforms in glucose transport in 3T3-L1 adipocytes: insignificance of atypical PKC. *Am J Physiol Endocrinol Metab* 283, E338-345.
- Veit, M., Geiger, H., Czygan, F.C., and Markham, K.R. (1990). Malonylated flavone 5-O-glucosides in the barren sprouts of *Equisetum arvense*. *Phytochemistry* 29, 2555–2560.
- Veys, K., Alvarado-Diaz, A., and De Bock, K. (2019). Measuring Glycolytic and Mitochondrial Fluxes in Endothelial Cells Using Radioactive Tracers. *Methods Mol Biol* 1862, 121–136.
- Virtanen, K.A., Peltoniemi, P., Marjamäki, P., Asola, M., Strindberg, L., Parkkola, R., Huupponen, R., Knuuti, J., Lönnroth, P., and Nuutila, P. (2001). Human adipose tissue glucose uptake determined using [(18)F]-fluoro-deoxy-glucose ([18F]FDG) and PET in combination with microdialysis. *Diabetologia* 44, 2171–2179.
- Waldén, T.B., Hansen, I.R., Timmons, J.A., Cannon, B., and Nedergaard, J. (2012). Recruited vs. nonrecruited molecular signatures of brown, “brite,” and white adipose tissues. *Am J Physiol Endocrinol Metab* 302, E19-31.
- Wang, Q., Jokelainen, J., Auvinen, J., Puukka, K., Keinänen-Kiukaanniemi, S., Järvelin, M.-R., Kettunen, J., Mäkinen, V.-P., and Ala-Korpela, M. (2019). Insulin resistance and systemic metabolic changes in oral glucose tolerance test in 5340 individuals: an interventional study. *BMC Med* 17, 217.
- Willcox, M.L., Graz, B., Falquet, J., Diakite, C., Giani, S., and Diallo, D. (2011). A “reverse pharmacology” approach for developing an anti-malarial phytomedicine. *Malar J* 10 Suppl 1, S8.
- World Health Organization (2013). WHO traditional medicine strategy: 2014-2023.
- Wueest, S., Rapold, R.A., Schumann, D.M., Rytka, J.M., Schildknecht, A., Nov, O., Chervonsky, A.V., Rudich, A., Schoenle, E.J., Donath, M.Y., et al. (2010). Deletion of Fas in adipocytes relieves adipose tissue inflammation and hepatic manifestations of obesity in mice. *J Clin Invest* 120, 191–202.
- Yang, J., Clark, A.E., Kozka, I.J., Cushman, S.W., and Holman, G.D. (1992). Development of an intracellular pool of glucose transporters in 3T3-L1 cells. *Journal of Biological Chemistry* 267, 10393–10399.
- Zhou, G., Myers, R., Li, Y., Chen, Y., Shen, X., Fenyk-Melody, J., Wu, M., Ventre, J., Doebber, T., Fujii, N., et al. (2001). Role of AMP-activated protein kinase in mechanism of metformin action. *J Clin Invest* 108, 1167–1174.

Figures

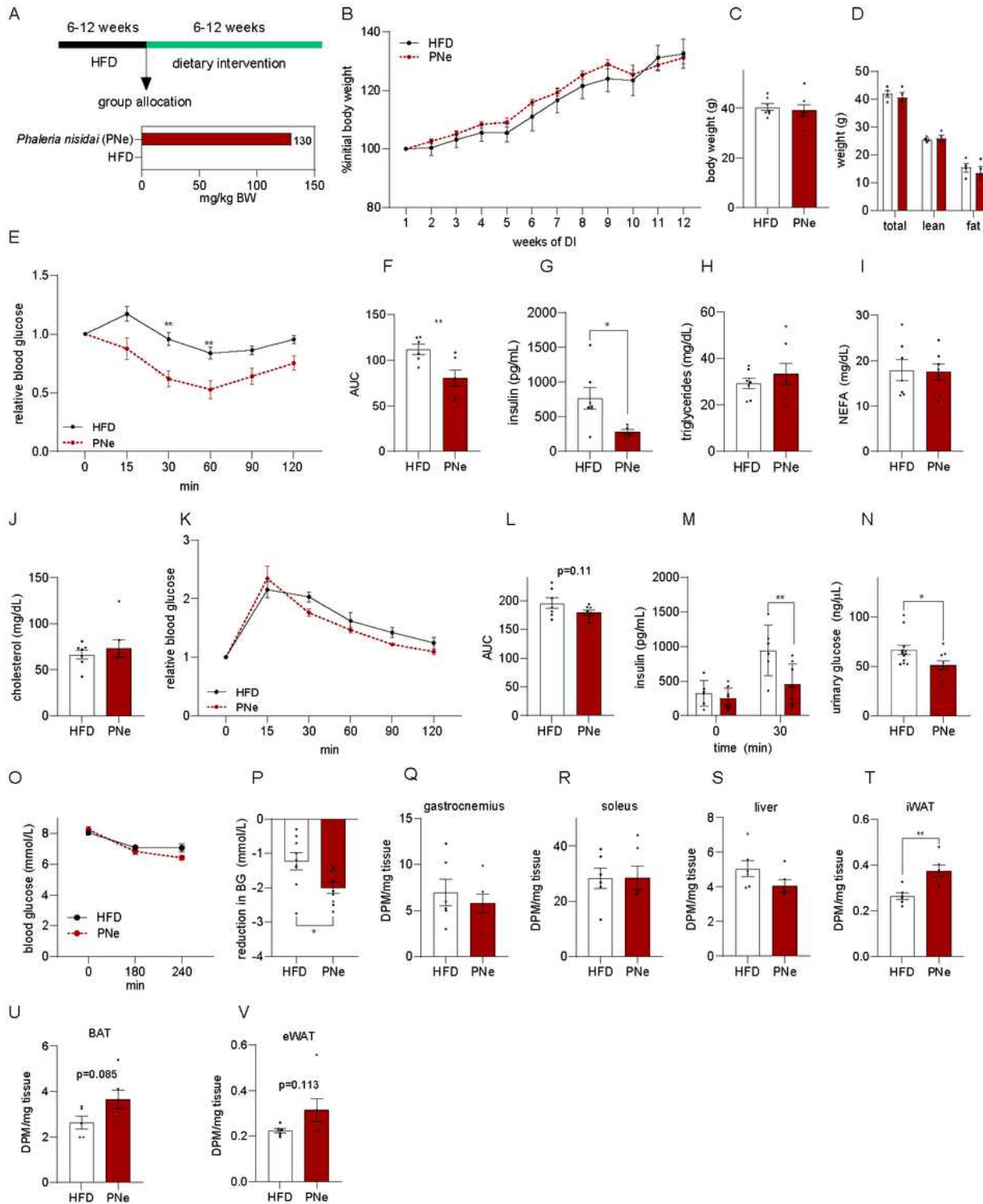


Figure 1

PNe alleviates glucose homeostasis in DIO mice.

(A) Schematic outlay of the dietary intervention (DI).

(B) Body weight development during DI as percentage of start weight.

(C) Final body weight after 7 weeks of DI.

(D) Body composition after 5 weeks of DI.

(E-F) (E) Insulin tolerance test and (F) corresponding AUC after 12 weeks HFD and 5 weeks DI. n=6

(G-J) Fasting (G) insulin, (H) triglyceride, (I) NEFA and (J) cholesterol concentrations after 12 weeks HFD and 7 weeks DI. n=5-8 per group

(K-L) (K) Oral glucose tolerance test and (L) corresponding AUC after 6 weeks HFD and 2 weeks DI. n=7-8 per group.

(M) Plasma insulin levels 30 min after an oral glucose load after 6 weeks HFD and 7 weeks DI. n=6-7 per group

(N) Urinary glucose concentration after 6 weeks HFD and 6 weeks DI. n=9-12 per group.

(O-P) (O) Blood glucose concentrations over time after an acute oral dose of PNe (130 mg/kg BW) vs vehicle after 10 days of HFD and (P) reduction in blood glucose levels from time point 240 mins vs baseline. n=9 per group. (Q-V) Tissue specific ¹⁴C-2-deoxyglucose glucose uptake into (Q) gastrocnemius, (R) soleus, (S) liver, (T) iWAT, (U) iBAT and (V) eWAT after 6 weeks HFD and 7 weeks DI. n=6 per group.

Results are reported as mean ± SEM. Two-tailed student's t-test for comparisons between two groups was applied in C, F-J, L, N, P-V. 2-way (D) or 2-way repeated measures ANOVA was applied in B-E, K, M and O with Sidak's post-hoc comparison. Statistical differences are indicated as *p<0.05, **p<0.01, ***p<0.001.

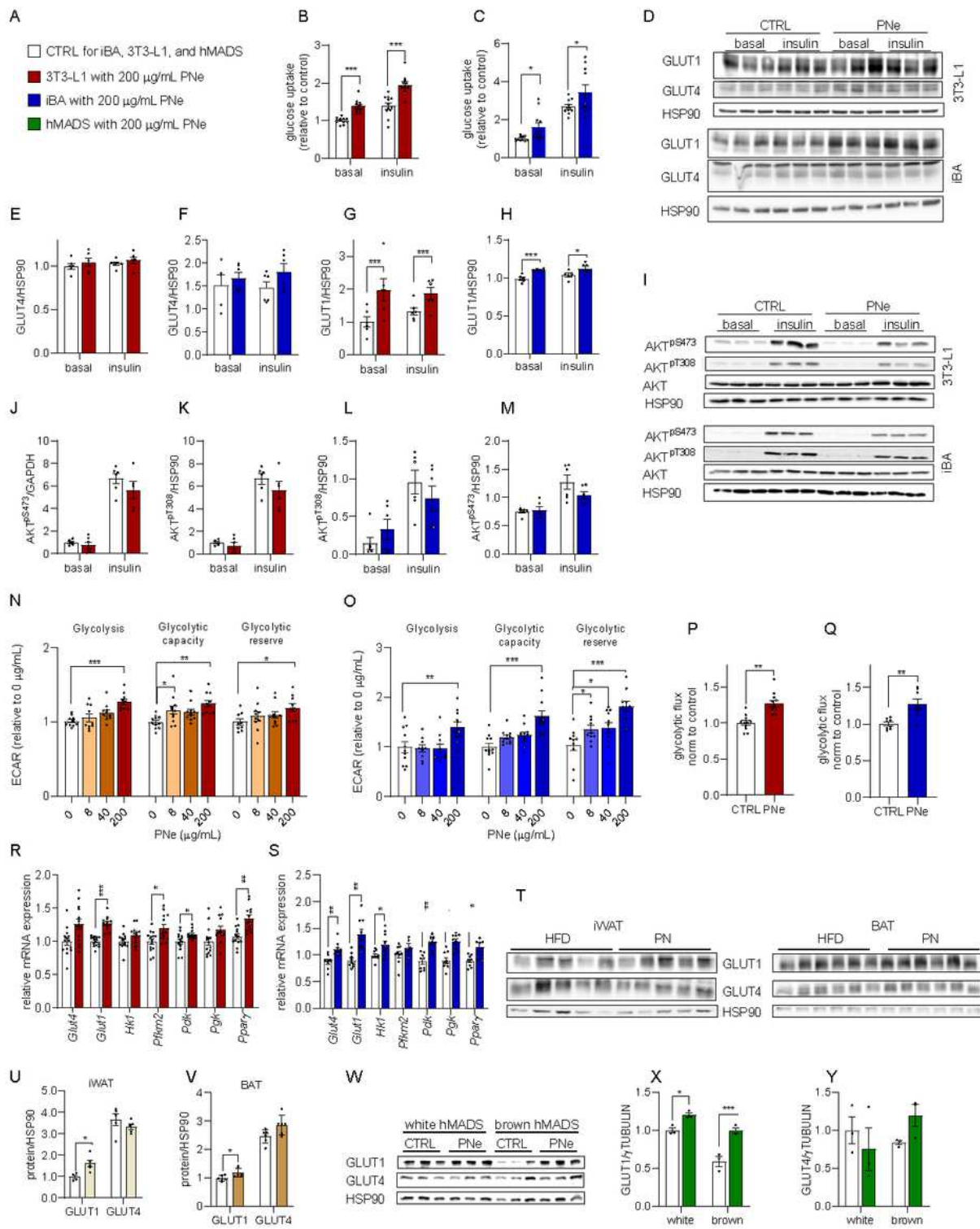


Figure 2

PNe increases adipocyte glucose uptake via insulin-independent GLUT1 *in vitro*.

(A) Color coding of bar graphs displayed in figures 2 and 3. 200 μ g/mL of PN was applied for 3 days in all experiments.

(B-C) Glucose uptake in basal and insulin-stimulated (100 nM, 60 min) condition in (B) 3T3-L1 and (C) brown adipocytes. (n=10-12)

(D-H) (D) Western blots for GLUT1 and GLUT4 in both adipocyte cell lines and (E-H) quantification. (n=6).

(I-M) (I) Western blots for AKT^{pS473} and AKT^{pT308} with or without insulin stimulation (20 min, 10 nM) in both adipocyte cell lines and (J-M) quantification. (n=6)

(N-O) Glycolytic stress test in (N) 3T3-L1 and (O) brown adipocytes. (n=11)

(P-Q) ³H-Glycolytic flux analysis of (P) 3T3-L1 and (Q) brown adipocytes. (n=8-12)

(R-S) Gene expression analysis of targets regulating glucose metabolism in (R) 3T3-L1 and (R) brown adipocytes. (n=9-14)

(T-V) (T) Western blots of glucose transporters in iWAT and BAT from mice after 12 weeks of DI and (U-V) quantification. (n=5-6)

(W-Y) Western blots of glucose transporter proteins in human brown and white hMADS and quantification of (X) GLUT1 and (Y) GLUT4. (n=3)

Results are reported as mean \pm SEM. Two-tailed student's t-test for comparisons between two groups was applied in P-Q, Multiple t-test with Holm-Sidak post-hoc test was applied in B-C, E-H, J-M, R-S, U-V and X-Y. 2-way ANOVA with Dunnett's post-hoc test was applied in N-O. All comparisons were performed against untreated control cells. Statistical differences are indicated as *p<0.05, **p<0.01, ***p<0.001.

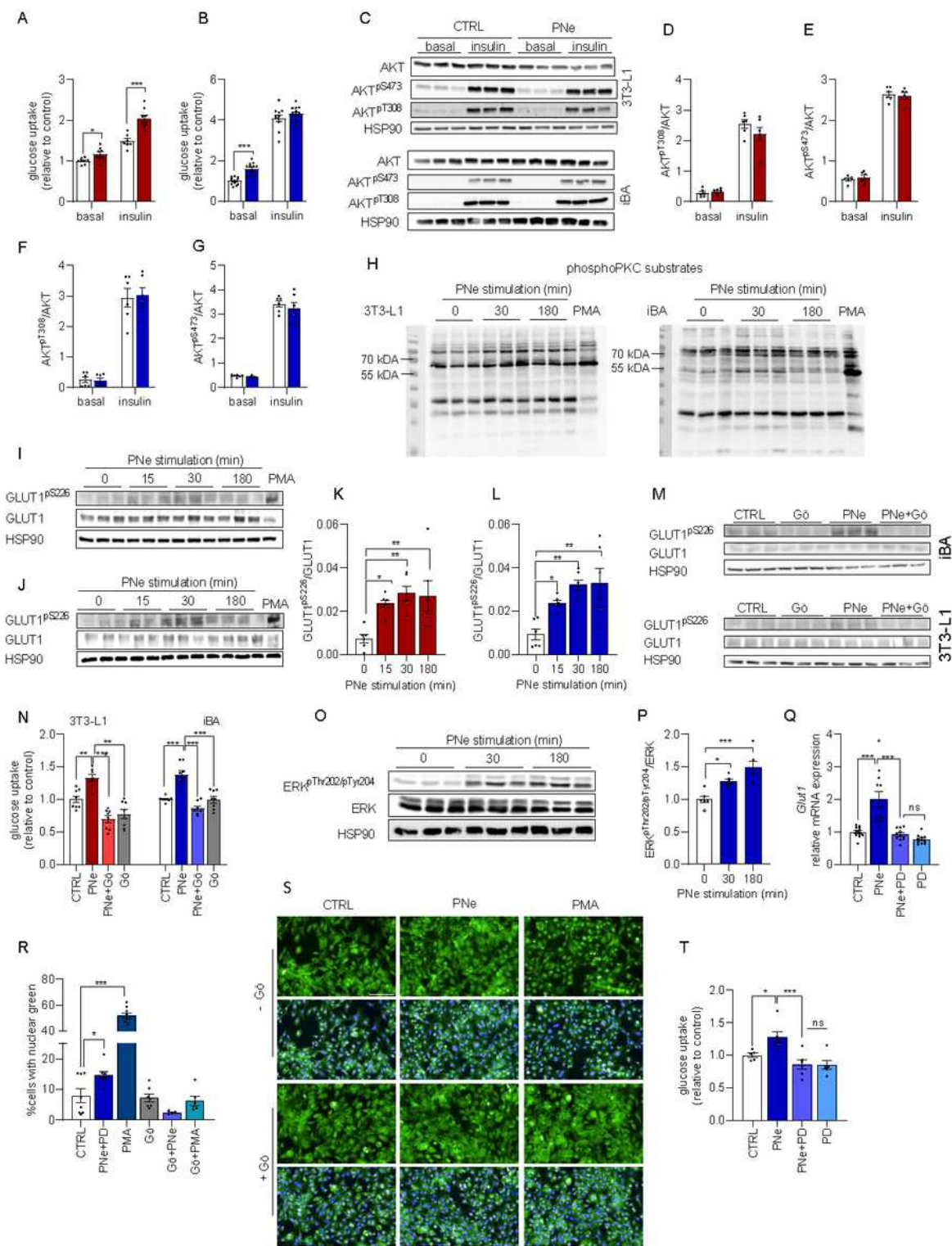


Figure 3

Short-term PNe activates the PKC-ERK1/2 axis.

(A-B) Glucose uptake in (A) 3T3-L1 and (B) brown adipocytes after acute PNe (colored bar) treatment (200 μ g/mL, 3 hours). n=8-9 per group.

(C-G) (C) Western blots for AKT^{pS473} and AKT^{pT308} in both adipocyte cell lines with or without insulin stimulation (10 nM, 20 min) and (D-G) quantification. n=6 per group.

(H) Pan phosphoPKC substrates antibody with PMA (250 nM) as positive control.

(I-L) Time course of GLUT1 phosphorylation at S226 following PNe treatment in (I) 3T3-L1 and (J) brown adipocytes and (K-L) quantification.

(M) Effect of PKC inhibition with Gö-6893 (30 min, 1 µM) on GLUT1^{pS226} levels following 3 hours of PNe stimulation.

(N) Glucose uptake assay with pretreatment of the PKC-inhibitor Gö-6893 (30 min, 1 µM) in 3T3-L1 and brown adipocytes. n=8 per group.

(O-P) (O) ERK1/2 phosphorylation at Thr204 and Tyr202 following PNe stimulation in brown adipocytes and (P) quantification of ERK^{pThr202/pTyr204}. n=6 per group.

(Q) *Glut1* mRNA levels in response to PNe exposure (4 hours) with or without pretreatment with the ERK1/2 inhibitor PD184352, 500 nM, 30 min). n=11-12 per group.

(R-S) (R) Quantification of ERK1/2 localization after PNe or PMA treatment (180 min) with or without PKC-inhibitor Gö-6893 (250 nM). (n=5-6 images per condition from 3 replicates with 200-250 cells per image). (S) Representative immunofluorescence pictures stained for nuclei (blue) and ERK1/2 (green) used for quantification in (R). Scale bar 100 µM.

(T) Glucose uptake after 16 hours of PNe with or without pretreatment by ERK1/2 inhibitor PD-98059 (500 nM, 30 min) in brown adipocytes. n=5-6 per group.

Results are reported as mean ± SEM. Multiple student's t-test with Sidak's post-hoc test was applied in A-B and D-G. One-way ANOVA with Dunnett's post-hoc test was applied in K-L and Q. One-way or two-way ANOVA with comparisons between all groups and Tukey's post-hoc test was applied in O, R-S and U. Statistical differences are indicated as *p<0.05, **p<0.01, ***p<0.001.

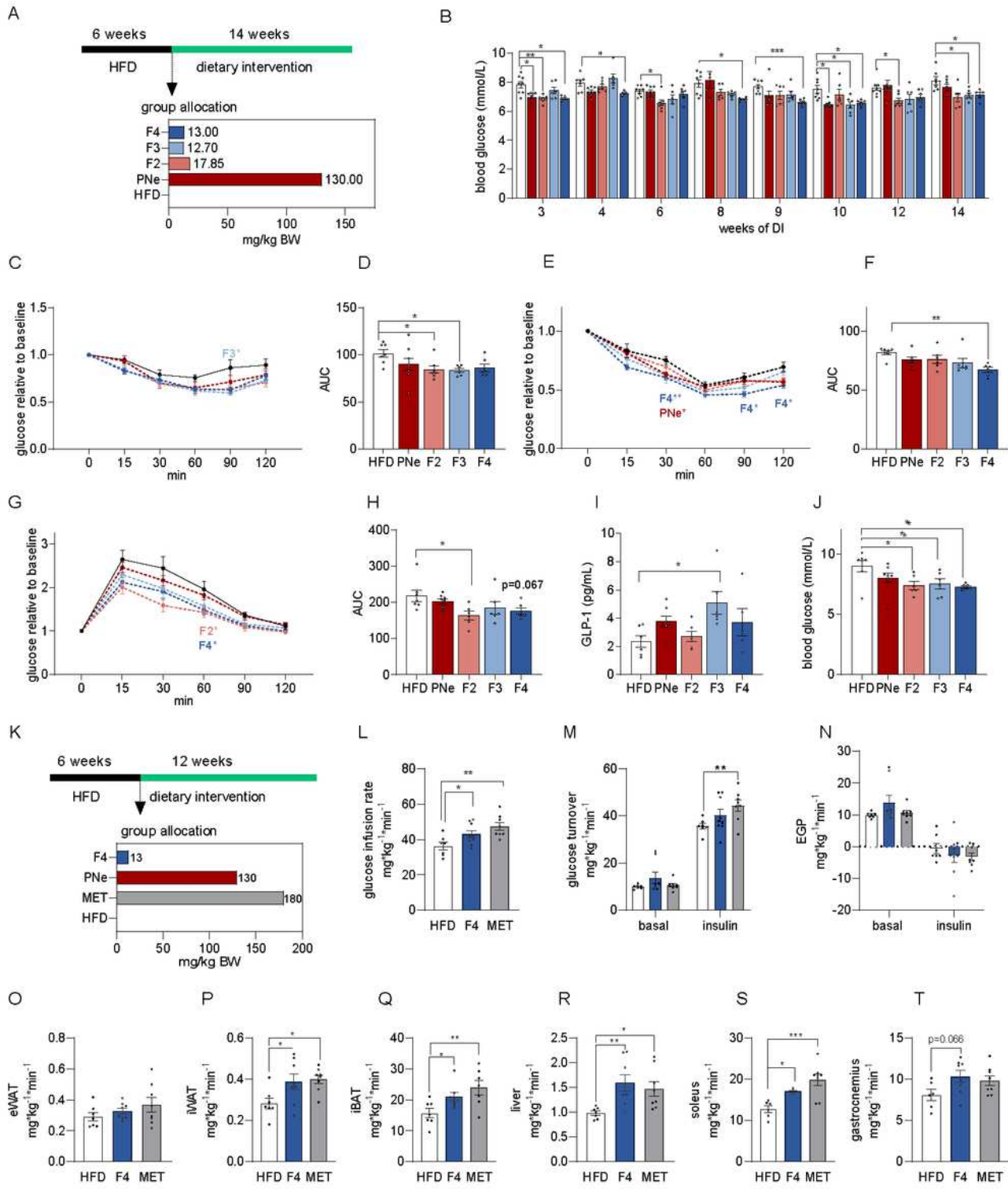


Figure 4

Bioactivity-guided fractionation of PNe reveals F4 as source of bioactive substances.

(A) Experimental set up of the dietary intervention (DI) and applied doses.

(B) Random fed blood glucose measured at 11 am. n=6-8 per group.

(C-F) (C) Insulin tolerance test and (D) AUC after 4 weeks of DI. (E) Insulin tolerance test after 10 weeks DI and (F) AUC. n=6-7 per group.

(G-H) (G) Oral glucose tolerance test (2g/kg BW) after 11 weeks DI and (H) AUC. n=6-8 per group.

(I) Circulating active GLP-1 levels 2 mins after an oral glucose load. n=6-7 per group.

(J) Fasting blood glucose concentrations at the end of the DI.

(K) Experimental set up of the DI with metformin (MET) as positive control drug. n=7-9 per group.

(L) Glucose infusion rates (GIR) at steady state during hyperinsulinemic-euglycemic clamps. n=7-9 per group.

(M) Basal and insulin-stimulated whole-body glucose turnover. n=7-9 per group.

(N) Endogenous glucose production (EGP) during basal and insulin-stimulated conditions. n=7-9 per group.

(O-T) Tissue-specific ^{14}C -2-deoxyglucose uptake rates into the (O) eWAT, (P) iWAT, (Q) iBAT, (R) liver, (S) soleus and (T) gastrocnemius. n=6-9 per group.

Results are reported as mean \pm SEM. One-way ANOVA with Dunnett (D, F, H, I, J) or Holm-Sidak's post-hoc (L, P-U) tests were applied for comparisons against HFD controls. Two-way ANOVA with Dunnett's post hoc test was applied in B-C, E, G and N-O. Statistical differences are indicated as * $p < 0.05$, ** $p < 0.01$.

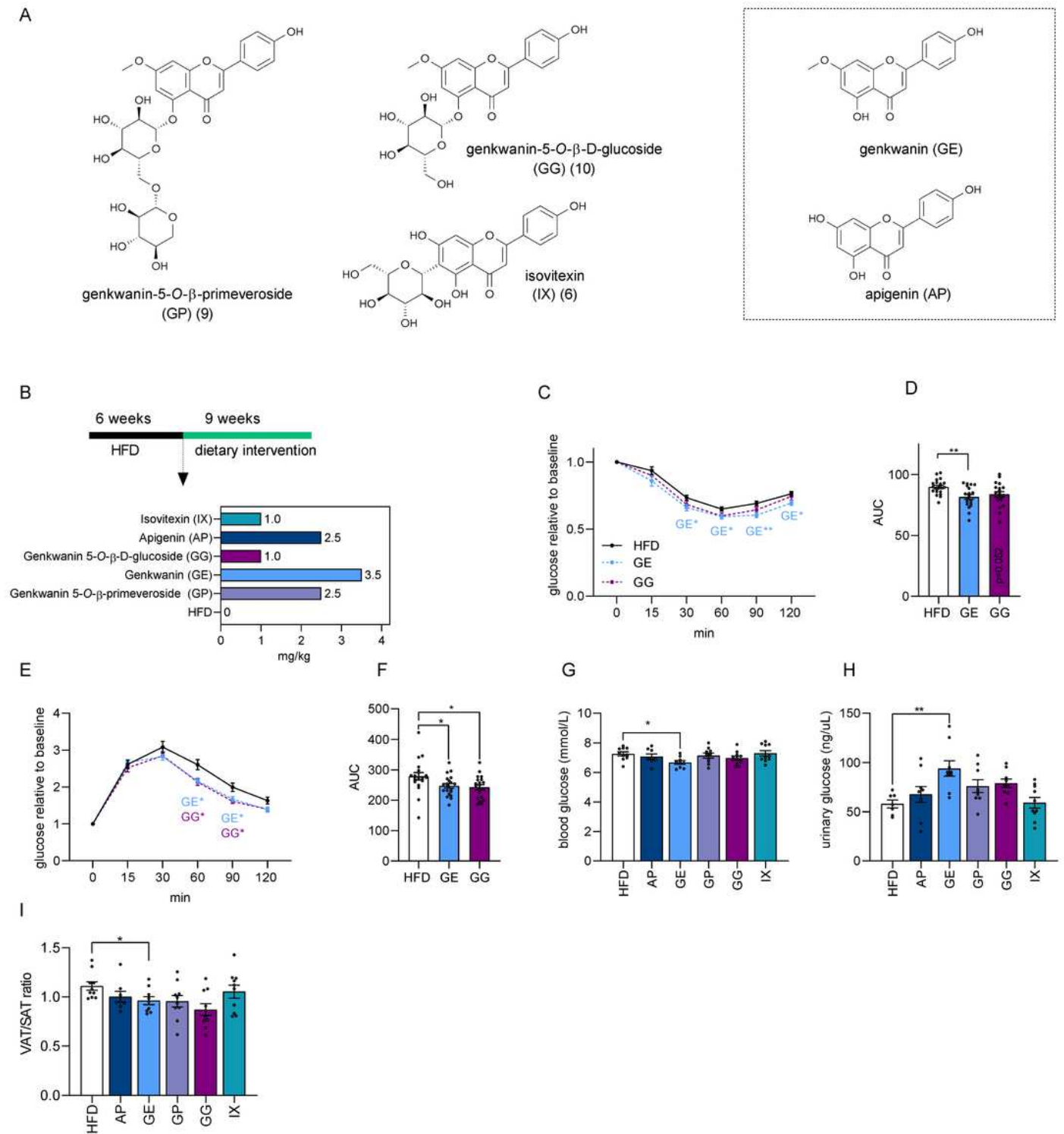


Figure 5

GE glycosides mediate the beneficial effects of F4.

(A) Structures of flavones tested *in vivo*, among which GP, GG and IX were isolated in F4, while GE and AP were selected as potential metabolites biotransformed in the digestive system after ingestion of the aforementioned constituents of F4.

(B) Experimental set up and applied doses during the DI.

(C-D) (C) Insulin tolerance test after 7 weeks of DI and (D) AUC. n=18-20 per group

(E-F) (E) Glucose tolerance test after 8 weeks of DI and (F) AUC. n=20 per group

(G) Random fed blood glucose concentrations after 9 weeks of DI. n=8-10 per group.

(H) Fasting urinary glucose concentrations after 4 weeks of DI. n=7-10

(I) Ratio of visceral (VAT) to subcutaneous (SAT). n=8-10 per group.

Results are reported as mean \pm SEM. Two-way ANOVA with Dunnett's post-hoc test was applied in C and D. One-way ANOVA with Dunnett's post-hoc test was applied in D and F-I. All comparisons were performed against HFD controls. Statistical differences are indicated as * $p < 0.05$, ** $p < 0.01$, *** $p < 0.001$.

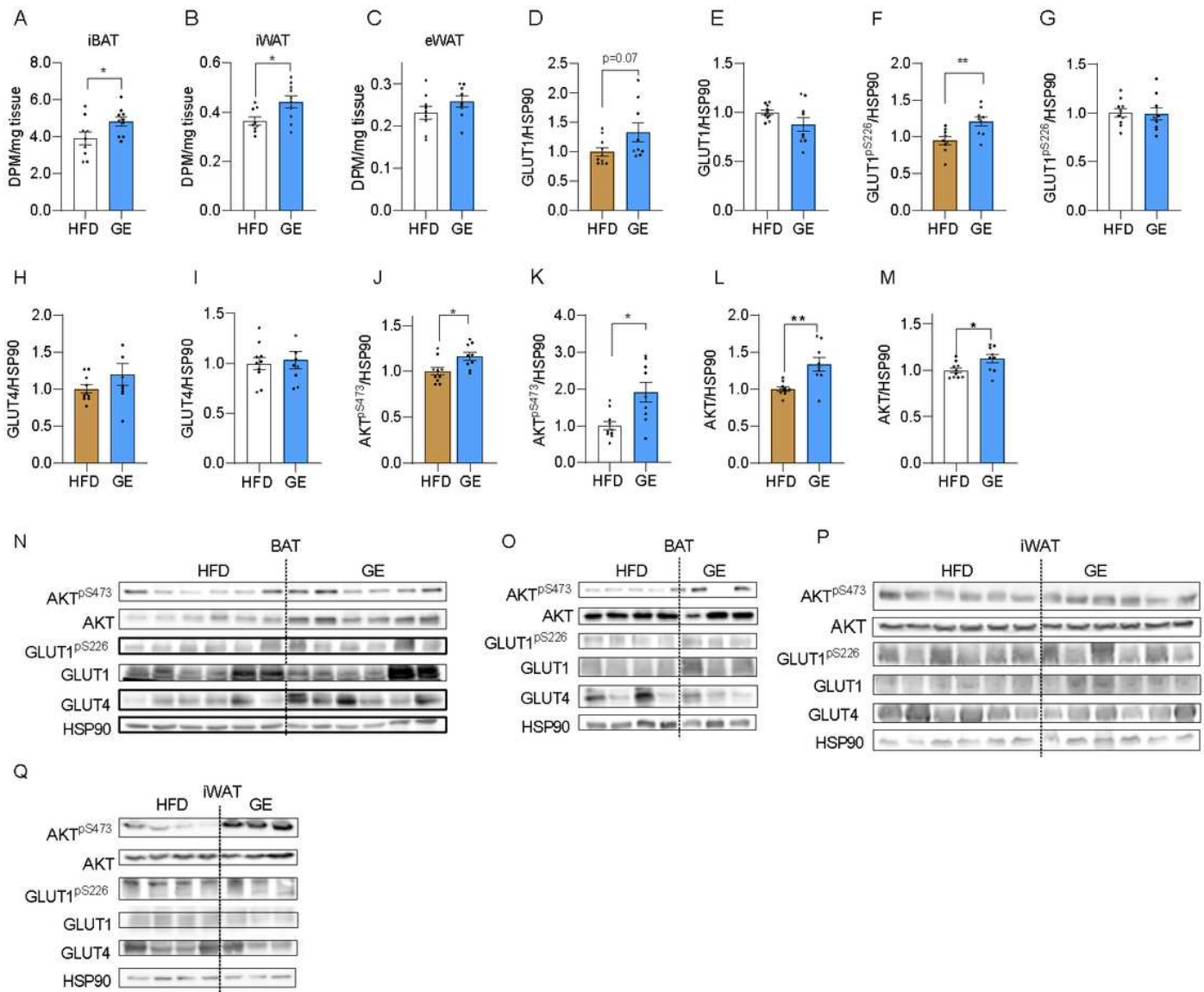


Figure 6

GE supports insulin action by promoting basal glucose uptake.

(A-C) ^{14}C -2-deoxyglucose uptake into (A) iBAT, (B) iWAT and (C) eWAT after 6 weeks HFD and 6 weeks DI. n=9-10 per group

(D-G) Effect of GE on (D-E) GLUT1 protein and (F-G) GLUT1 phosphorylation at S226 in the iBAT (brown bar) and iWAT (white bar). n=9-10 per group.

(H-I) Effect of GE on GLUT4 protein in the (H) iBAT and (I) iWAT. n=9-10 per group.

(J-M) Effect of GE on (J-K) AKT phosphorylation at S473 and (L-M) total AKT levels in iBAT (brown bars) and iWAT (white bars). n=9-10 per group.

(N-Q) Western blots quantified in D-M from (N-O) BAT and (P-Q) iWAT of random fed animals after 9 weeks DI. n=9-10 per group.

Results are reported as mean \pm SEM. Two-tailed student's test was applied in all comparisons. Statistical differences are indicated as * p <0.05, ** p <0.01.

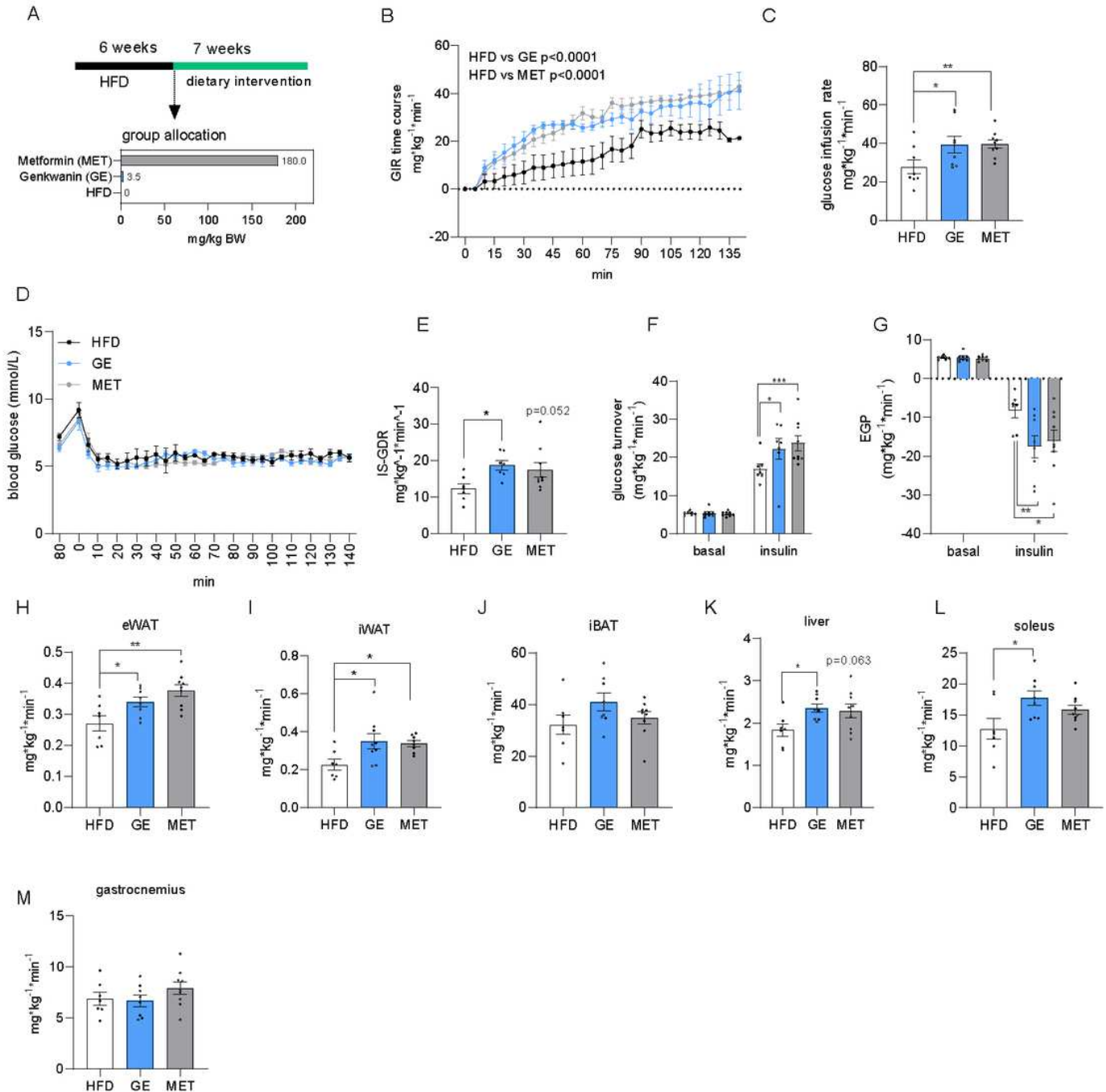


Figure 7

GE competes against metformin in hyperinsulinemic-euglycemic clamps.

(A) Experimental set up for hyperinsulinemic-euglycemic clamps.

(B and C) (B) Glucose infusion rate (GIR) over the course of the clamps and (C) GIR during the steady state condition. n=7-9 per group.

(D) Blood glucose concentration during the clamp procedure. n=7-9 per group

(E) Insulin-stimulated glucose disappearance rate (IS-GIR) at steady state condition. n=7-9 per group

(F and G) (F) Whole body glucose turnover and (G) endogenous glucose production (EGP) during basal and insulin-stimulated states. n=7-9 per group.

(H-M) ^{14}C -2-deoxyglucose uptake into (H) eWAT, (I) iWAT, (J) iBAT, (K) liver, (L) soleus and (M) gastrocnemius after 35 min into steady state. n=7-9 per group

Results are reported as mean \pm SEM. One-way ANOVA with Dunnett's post-hoc test was applied in figures C, E and H-M. Two-way ANOVA with Dunnett's post-hoc test was applied in figures B, F and G. All comparisons were performed against HFD controls. Statistical differences are indicated as * $p < 0.05$, ** $p < 0.01$, *** $p < 0.001$.

Supplementary Files

This is a list of supplementary files associated with this preprint. Click to download.

- [Supplementalinformation.pdf](#)